

**THERMAL INFRARED DATA ANALYSES OF METEOR CRATER, ARIZONA:
IMPLICATIONS FOR MARS SPACEBORNE DATA FROM THE
THERMAL EMISSION IMAGING SYSTEM**

by

Shawn Patrick Wright

BS, Geology, Sul Ross State University, 2000

Submitted to the Graduate Faculty of

Arts and Sciences in partial fulfillment

of the requirements for the degree of

Master of Science

University of Pittsburgh

2003

Thermal Infrared Data Analyses of Meteor Crater, Arizona: Implications for Mars Spaceborne Data from the Thermal Emission Imaging System

Shawn P. Wright, M.S.

**Department of Geology and Planetary Science
University of Pittsburgh, 2003**

Thermal infrared (TIR) data from the Advanced Spaceborne Thermal Emission and Reflection Radiometer (ASTER) instrument are used to identify the lithologic distribution of the Meteor Crater ejecta blanket and nearby (within ~3 km) region. This has many applications to the analysis of data from the Thermal Emission Imaging System (THEMIS) instrument that is currently in orbit at Mars. ASTER and THEMIS, whereas orbiting different planets, have similar spatial and spectral resolutions. THEMIS represents the highest spatial resolution (100 m) to date of the Martian surface, thereby allowing small (~ 1km) impact craters to be studied in detail for the first time. Meteor Crater serves as an analog for the many similar-sized impact sites on the surface of Mars. These sites are future research targets with THEMIS, and ASTER data of Meteor Crater provides ideal data and geologic landscape in preparation for future THEMIS investigations. Fieldwork at Meteor Crater yielded sample collection of the primary lithologies and an opportunity to validate previously-collected high-resolution (3.2 m), airborne Thermal Imaging Multispectral Scanner (TIMS) data. Laboratory thermal emission spectra were obtained for the samples collected. Deconvolution of ASTER TIR emissivity data were performed with image end-members and sample end-members. Comparisons of the spaceborne data to high-resolution airborne TIMS data were used to assess the validity of the ASTER end-member analyses. The ASTER image end-member analysis agreed well with the earlier TIMS end-member analysis where the effects of resolution degradation were accounted for. Laboratory spectra and mineral spectral libraries provided poor fits of deconvolution of multispectral TIR data. Lithologies with similar spectral signatures or with low areal abundances were difficult to identify.

Using the same methodology as that applied to the ASTER TIR data of Meteor Crater, THEMIS TIR data of a small (~ 1 km) impact crater in Syrtis Major were analyzed. The crater's rim and ejecta blanket was found to contain larger particle sizes than the surrounding (ejecta-free) plain, indicating a young (fresh) impact age and little or no accumulation of dust. The composition of the rim, ejecta, and surrounding plain was determined to be basaltic. It is hoped that the work performed here will complement future investigations of fresh impact sites with THEMIS data that may be used to solve geologic questions such as 1.) the composition of ejecta blocks that represent pre-impact, underlying stratigraphy in high-albedo, dust-covered regions of Mars, 2.) the approximate age of impact, and 3.) regolith/dust thickness, which appears to be a factor of #2.

ACKNOWLEDGEMENTS

This study would not have been possible with the help of a few organizations and many individuals. The author would like to thank the personnel of Barringer Crater Company and Meteor Crater Enterprises for allowing field research to be conducted. Thesis advisor Michael Ramsey provided guidance, patience, and financial support while answering countless questions before, during, and after field research. William Cassidy and Ian Skilling were very helpful as committee members. Time spent performing research with the thermal infrared spectrometer at the Arizona State University Mars Space Flight Facility was made possible by Phil Christensen and Steve Ruff. Thanks to Steve Ruff and Amy Knudsen for answering questions about data analysis of thermal emission spectra. Frank Seelos provided much-needed deconvolution of our ENVI data. Finally, I would like to thank the personnel of the Image Visualization and Infrared Spectroscopy (IVIS) Laboratory, which included Sally Kuhn, Tamara Misner, Jeff Mihalik, and Jessica Bluth for all the encouragement, friendship, and technical support.

TABLE OF CONTENTS

Abstract	
Section 1. Introduction	1
Section 2. Background	3
2.1. Geology of Meteor Crater, Arizona	3
2.2. Thermal infrared spectroscopy	8
2.2.1. Calculation of Emissivity	10
2.2.2. Spectral Deconvolution Analysis	12
2.3. Instrument Descriptions	13
2.3.1. ASTER	13
2.3.2. TIMS	15
2.3.3. THEMIS	15
2.4. Thermal infrared remote sensing	16
2.4.1. Earth	17
2.4.2. Terrestrial analogs and Instrumental Proxies	17
2.4.3. Mars	17
2.4.4. Use of image end-members	20
2.5. Mars Impact Craters	21
2.5.1. A small impact crater in Syrtis Major	23
Section 3. Methodology	25
3.1. Acquisition and Processing of ASTER TIR data	25
3.2. Selection of Image End-members	26
3.3. Sample Collection and Emission Spectra of Meteor Crater Lithologies	27
3.4. Linear Spectral Deconvolution	29
3.5. Acquisition and Processing of TIMS data	30
3.5.1. Selection of TIMS image end-members	31
3.6. Description of Regions of Investigation at Meteor Crater	31
3.7. Acquisition and Processing of THEMIS TIR data	33
3.8. Selection of a small, fresh impact site in Syrtis Major	35

Section 4. Results	36
4.1 ASTER TIR end-member analyses	36
4.1.1 Image end-member analysis	36
4.1.2 Sample end-member analysis	38
4.2 TIMS image end-member analysis	39
4.3 Discussion	40
4.3.1 Comparison of ASTER end-member analyses	40
4.3.2 Investigation of remote sensing properties	42
4.4. THEMIS TIR data	45
4.4.1. Temperature data	45
4.4.2. Emissivity data and image end-member analysis	46
Section 5. Conclusions	48
Figures	51
Tables	84
Bibliography	90

LIST OF FIGURES

Figure 1.	The region surrounding Meteor Crater, Arizona	51
Figure 2.	ASTER VNIR image of Meteor Crater	52
Figure 3.	Stratigraphic Column	53
Figure 4.	Geologic Map of Meteor Crater	54
Figure 5.	Contour Map of Meteor Crater	55
Figure 6.	Post-impact lake	56
Figure 7.	TIR spectra of common minerals	57
Figure 8.	TIR spectra of quartz of varying particle sizes	58
Figure 9.	ASTER TIR spectral response functions	59
Figure 10.	ASTER DEM of Meteor Crater	60
Figure 11.	THEMIS TIR spectral response functions	61
Figure 12.	Coverage of THEMIS TIR scene I01297001	61
Figure 13.	THEMIS TIR scene I01297001 radiance data	62
Figure 14.	Coverage of THEMIS TIR scene I01852006	63
Figure 15.	THEMIS TIR scene I01852006 radiance data	64
Figure 16.	Coverage of ASTER TIR scene of Meteor Crater	65
Figure 17.	5-Dimensional cluster of ASTER emissivity data	66
Figure 18.	Spectral plot of ASTER TIR image end-members	66
Figure 19a.	Spectral plots of laboratory samples from Meteor Crater	67
Figure 19b.	Laboratory spectra convolved to ASTER filter functions	67
Figure 20a.	ASTER TIR image end-member analysis	68
Figure 20b.	1% stretch of ASTER TIR image end-member analysis	68
Figure 21a.	ASTER TIR sample end-member analysis	69
Figure 21b.	1% stretch of ASTER TIR image end-member analysis	69
Figure 22a.	Close-up of CEB of Figure 20b	70
Figure 22b.	Close-up of CEB of Figure 21b	70
Figure 23.	Spectral plot of TIMS image end-members	71
Figure 24.	Spectral plot of THEMIS TIR image end-members	72
Figure 25.	RMS error image of ASTER TIR image end-member analysis	73
Figure 26.	RMS error image of ASTER TIR sample end-member analysis	74
Figure 27.	Example of GPS data on ejecta lobe	75
Figure 28.	TIMS image end-member analysis	75
Figure 29.	RMS error image of TIMS image end-member analysis	76
Figure 30.	THEMIS daytime and nighttime temperatures of Syrtis	77
Figure 31.	Emissivity scene of SW Syrtis Major Planitia	78
Figure 32a.	THEMIS image end-member analysis (0% stretch)	79
Figure 32b.	THEMIS image end-member analysis (1% stretch)	79
Figure 33a.	Extent of CEB shown in Figure 33b	80
Figure 33b.	Close-up of deconvolution of CEB	80
Figure 34.	RMS error image of THEMIS image end-member analysis	81
Figure 35.	RMS error image of THEMIS image end-member analysis (stretched from 2% – 3%)	82
Figure 36.	Close-up of CEB of RMS error image of THEMIS image end-member analysis	83

LIST OF TABLES

Table 1.	Mars TIR instruments	84
Table 2.	ASTER instrument specifications	85
Table 3.	TIMS TIR band centers	86
Table 4.	THEMIS instrument specifications	86
Table 5.	ASTER TIR data sets of Meteor Crater	87
Table 6.	Comparison of Areal Abundances of ASTER end-member analyses	88
Table 7.	Comparison of TIMS and ASTER end-member analyses	90

1. Introduction

Where applicable, remote sensing using the thermal infrared (TIR) wavelength region ($\sim 3 \mu\text{m}$ to $50 \mu\text{m}$) has been shown to provide compositional properties of planetary surfaces [Gillespie *et al.*, 1984; Hook *et al.*, 1994; Bandfield *et al.*, 2000; Hamilton and Christensen, 2000]. This is due to silicates, carbonates, and other common rock-forming minerals having unique spectral characteristics in the TIR wavelength region [Salisbury and Walter, 1989]. Further, with the exception of fine ($< \sim 60 \mu\text{m}$) particles, TIR data are linearly additive [Ramsey and Christensen, 1998].

Where surface volcanic processes have ceased, impact cratering is the dominant geologic process that modifies the surfaces of Mars, Mercury, and the Moon. Impact craters can serve as probes into the subsurface by exposing underlying lithologies. Analyses of their characteristics can potentially infer the target (surface) properties and the climatic conditions since formation [Greeley and Iverson, 1985; Grant, 1990]. Over 42,000 impact craters with diameters greater than 5 km have been catalogued for the surface of Mars [Barlow, 2000]. Recent publications estimate that there are approximately a quarter of a million impact sites on Mars that are ≈ 1 km in diameter [Morton, 2002].

Dust covers the surfaces of the high-albedo regions of Mars [Christensen, 1982, 1986]. The mineralogy of low-albedo (i.e. non-dusty) regions on Mars has been characterized in detail and used in the determination of the geologic history of the region [Bandfield *et al.*, 2000; Christensen *et al.*, 2000a, 2000b, 2001; Bandfield, 2002]. However, the high-albedo, dusty regions have not been as extensively studied. This is due to the fact that the TIR spectra of small particles ($< 60 \mu\text{m}$) such as dust are not

linearly additive and therefore not easily interpreted [*Ramsey and Christensen, 1998*]. Recent studies have investigated the mineralogy of the martian dust [*Ruff and Christensen, 2002; Bandfield et al., 2003*], but this information is not indicative of regional geology due to the homogeneous nature of the dust. There exist useful studies of dust and its TIR interpretations in accordance with Mars data sets [*Johnson et al., 2002a*]. In that study, the interpretation of TIR data of dust-covered surfaces was investigated in preparation for analyzing TIR data of the high-albedo regions.

This study seeks to describe, find, and analyze localized areas in low-albedo regions where large accumulations of dust are not present. Fresh impact craters should expose large particle sizes such as boulders, cobbles, and sand in their rims and pristine ejecta blankets. Further, if recently formed, there should not be a large enough accumulation of dust to affect TIR spectra analysis [*Wright and Ramsey, 2002, 2003*]. According to diagrams of crater size vs. frequency, small impact sites outnumber the larger variety on unmodified planetary surfaces and should be of younger age [*Melosh, 1989*].

TIR data from the Thermal Emission Imaging System (THEMIS) represent the highest spatial resolution (100 m) of the martian surface over the TIR wavelengths. Before its advent, it was impossible to determine the compositional and thermophysical properties of the rims and ejecta blankets of small (1-2 km diameter) impact craters on Mars. The Advanced Spaceborne Thermal Emission and Reflection Radiometer (ASTER) provides multispectral TIR data of Meteor Crater, Arizona over similar spatial and spectral resolutions to those of the THEMIS instrument.

This study represents the TIR analysis of ASTER data of Meteor Crater as a proxy for examining THEMIS TIR data of similar craters on Mars. The objective of the work is to investigate the accuracy of deconvolving multispectral TIR data with image end-members and determine if martian impact sites can be studied in a similar way with THEMIS TIR data. As discussed above, small (1-2 km diameter) impact craters are abundant on all geologic terrains on Mars [Carr, 1981]. A recently-formed impact site in Syrtis Major, Mars was chosen for TIR analysis with THEMIS data using the same methodology employed with the ASTER TIR data of Meteor Crater.

Section 2 describes the background information about the geology of Meteor Crater, TIR spectroscopy, TIR remote sensing, and the TIR instruments needed to understand the following sections. Section 2 also introduces a small impact crater in Syrtis Major, which is examined with THEMIS TIR data. The methodology of this study is described in section 3 and results are discussed in section 4. The work is concluded in section 5.

2. Background

2.1 Geology of Meteor Crater, Arizona

Meteor Crater is located in north-central Arizona near the Canyon Diablo in the southern part of the Colorado Plateau at approximately $35^{\circ} 01' N$, $111^{\circ} 01' W$ (Figure 1). The crater was created 49,000 years ago by the impact of a 30-50 m bolide into sediments of the Mesozoic and Paleozoic Eras [Nishiizumi *et al.*, 1991]. The impact produced a simple, bowl-shaped crater that has an average diameter of 1186 m, with a rim crest to floor depth of 167 m, or 30-60 m above the surrounding plain. The climate is semi-arid

with sparse vegetation and rock exposures are exceptionally good. The lack of abundant vegetation and semi-arid climate make the area ideal for thermal infrared remote sensing (Figure 2).

In the region surrounding the crater, the Colorado Plateau has a low relief ($<5^\circ$) and the surface consists of relatively flat-lying beds of Permian and Triassic age. The crater is located near the apex of one of several monoclinical folds in this region. Beds are offset by wide-spaced NW-SE trending normal faults that have lengths of many kilometers but displacements of a few to 30 meters [Shoemaker, 1963]. Two mutually perpendicular sets of vertical joints trending NE-SW and NW-SE are responsible for the squarish appearance of the crater. The NE-SW set combines with the local 5° dip to the NE to control the trend of the secondary stream directions in this area, as shown in Figure 1.

Meteor Crater features beds ranging in age from the Coconino Sandstone of the Permian Period to the Moenkopi Formation of the Triassic Period (Figure 3). The basement consists of Pennsylvanian and Permian-aged Supai Formation. The Supai Formation is a clay-rich, red, fine-grained, argillaceous sandstone interbedded with yellow subordinate siltstone. The Supai Formation was not sampled by the impact that produced Meteor Crater and therefore is not contained within the crater's ejecta blanket or rim. The overlying Coconino Sandstone consists of fine-grained, saccharoidal, white, cross-bedded, eolian sandstone [McKee, 1934]. This lithology represents the remains of dune fields from over 265 million years ago. The sandstone is well-sorted, containing $>97\%$ quartz [Horz *et al.*, 2000]. The Coconino has a thickness of 210-240 m, but only the upper 80 m was sampled by impact.

The Coconino Sandstone is overlain by the Permian Toroweap Formation. The Toroweap is a white to yellowish-brown, coarse-grained sandstone with interbeds of a reddish mudstone and dolomite [McKee, 1938]. Its stratigraphic thickness is 2.7 m. The dolomitic interbeds of the Toroweap were the floor of a shallow sea that migrated in from the west. The sandy portions represent a transgressing and regressing ancient shoreline over 255 million years ago. Due to its small stratigraphic thickness and consequent limited areal abundance in the crater's rim and ejecta, the Toroweap is grouped with the Coconino Sandstone for the purpose of this study. Further, the two have similar spectral signatures over the thermal infrared wavelengths used in this study.

Conformably overlying the Toroweap is the Permian Kaibab Formation. The Kaibab Formation is a fossiliferous dolomite and dolomitic limestone. Three members are recognized [McKee, 1938]. The lower two members, known as the Gamma and Beta members, are composed of massive, dense dolomite. The upper member is known as the Alpha member and consists of well-bedded limestone and dolomite with limited thin sandstone interbeds. The Kaibab was deposited in a low-energy, shallow marine environment over 250 million years ago. The entire lithology measures 79.5 to 81 meters in thickness. The stratigraphic thickness of the Kaibab Formation in the vicinity of Meteor Crater is well-constrained by studies of cores drilled in and around the crater and the ejection of the entire lithology upon impact.

Unconformably overlying the Kaibab is a thin, patchy veneer of Moenkopi Formation of Triassic age. To the west of the crater beyond Canyon Diablo, the Moenkopi has been completely eroded, leaving the Kaibab Alpha Member as the surface. The Moenkopi Formation has two members in the vicinity of Meteor Crater and increases

in thickness as it extends to the east. The lower Wupatki Member is a fine-grained, pale, reddish-brown sandstone that measures 0.3 to 1.0 m in thickness. The upper Moqui Member is a dark, reddish-brown, fissile siltstone that is 3 to 6 m thick [McKee, 1954]. The impact resulted in an overturning of the beds as they were ejected. Therefore, nine to fifteen meters of Moenkopi strata are exposed in the walls of Meteor Crater [Shoemaker & Kieffer, 1974]. Bedrock of Moenkopi contain ripple marks and were likely deposited on a coastal floodplain over 200 million years ago.

The surface exposures of each original and ejected lithology have been mapped in detail by Shoemaker [1960, 1963]. A geologic map from the work is shown as Figure 4. The physical characteristics of the crater are shown in a USGS contour map as Figure 5.

Scissor faults located in the corners of the crater have caused uplift to various degrees in each crater wall. As a result, the exposures of each of the three primary lithologies within the inner-crater walls and rim are not uniform. Coconino Sandstone is observed on the eastern, northern, and southern walls, but is not found on the western wall. Where the crater walls meet the floor, there is talus formed from the erosion of lithologies in the wall above. A slump in the northwest corner produced an elevated terrace on the crater floor.

The uppermost layer on the crater floor consists of talus and Quaternary alluvium composed of clasts of the Permian and Triassic lithologies described above. A minor amount of basaltic ash from the nearby San Francisco volcanic field is also apparent in the floor's silt sediments. Toward the center of the crater floor, lake beds from the late Pleistocene Epoch and playa beds from the Holocene Epoch indicate that the crater was a post-impact lake that has dried up as the climate turned semi-arid. Drill cores near the

center of the crater reveal ~30 m of Pleistocene lake beds and alluvium underlying 1-2 m of Holocene playa beds and alluvium [*Shoemaker and Kieffer, 1974*]. Beneath the Pleistocene sediments are a mixed debris unit and a mixed breccia layer that contain shocked rocks and oxidized meteoritic material. These units are thoroughly mixed and fused and grade upwards to finer grain sizes. *Shoemaker [1963]* and *Shoemaker and Kieffer [1974]* interpret this to represent the fallout of high-temperature debris that was thrown in the air and then settled and cooled on the crater floor. Figure 6 depicts the uplifted strata of the crater rim, impact breccia on the crater floor, and the post-impact lake.

Large boulders and cobbles of the three main lithologies have been deposited on the crater rim. Each lithology dominates a radial sector of the crater rim due to the near-horizontal scissor faults in the corners of the crater and the effects of erosion. The near-horizontal strata that were located at or near the point of impact have been uplifted and folded back with the uppermost layer of Moenkopi being folded back on itself.

Shoemaker [1963] described the rim and near-rim debris as “peeled away” like the petals of a flower. Erosion of the rim since crater formation has resulted in the “hinge line” of the fold not always being apparent on the rim.

The continuous ejecta blanket (CEB) consists of fragments of the three principal stratigraphic units, but inverted and preserved up to 2 crater radii (CR) from the rim. The near-rim CEB is hummocky and consists of blocks ranging in size from 0.5 to 30 m. With the exception of the southern ejecta flap, the majority of the ejecta are blocks of the Kaibab Fm. with lobes of Coconino Ss. on the northern and northeastern ejecta blanket. To the south and southeast of the crater, the ejecta blanket is composed almost entirely of

Coconino Ss. that shows varying degrees of shock metamorphism [*Shoemaker and Kieffer, 1974*]. Ejecta lobes of Coconino and Kaibab can be described as unconsolidated. To the north and northeast, drainages along radial gullies have transported a portion of the original near-rim CEB to mantle the outer CEB [*Grant and Schultz, 1993*]. To the west of the crater, the CEB has been mantled by fines of Kaibab transported by southwesterly winds [*Garvin et al., 1989*]. Southwesterly winds are also responsible for the northeast-trending windstreak that is evident in aerial photos and remote imaging (Figure 2). The source of the windstreak is the Coconino Ss. ejecta on the southern rim [*Grant and Shultz, 1993; Ramsey, 2002a*]. The windstreak's composition and source are discussed thoroughly under the TIR interpretations of the TIMS and ASTER data of the crater (section 4).

2.2 Thermal Infrared Spectroscopy

Thermal infrared (TIR) spectroscopy is based upon the principle that a crystalline lattice will selectively absorb certain wavelengths in a TIR spectrum that correspond to the vibrational frequencies of its constituent atoms and molecules [*Kendall, 1966*]. These are evident as spectral absorption bands. The specific wavelengths and strengths are characteristic of the chemical composition and unique structure of the material under examination [*Hall, 1947*]. All minerals display a unique spectral signature over the TIR wavelengths (~3 to 50 μm) due to the stretching and bending vibrations of atoms in the crystal lattices of minerals [*Houghton and Smith, 1966*]. These vibrational motions occur at specific, quantized frequencies, and where incident electromagnetic energy corresponds to one of these frequencies, the result is the excitation of a vibration and an

absorption feature in the TIR spectrum. All silicates, carbonates, sulfates, oxides, phosphates, and hydroxides have TIR spectral features associated with the vibrational motions of their components due to the polymerization of different anion groups such as SiO₄, CO₃, SO₄, and PO₄ [Kendall, 1966; Salisbury and Walter, 1989]. A mineral's bond strength, bond length, cation coordination, and anion composition all affect and influence the vibrational energy and therefore the number, relative strength, and wavelength positions of the spectral absorptions. The ability to identify mineralogy and interpret composition lends itself to remote observation of compositional interpretation.

Silicates constitute approximately 95% of minerals exposed at the Earth's surface [Berry *et al.*, 1983]. As the polymerization of the SiO₄ tetrahedra changes from isolated tetrahedral to chain, sheet, and framework silicates, the wavelength of the absorption feature changes. As the bond strength and mineral structure is changed, so, too, is the spectral absorption feature. See Figure 7 adapted from Christensen *et al.* [1992] for spectra of common framework, sheet, chain, and isolated tetrahedral silicates. The thermal infrared properties of silicates are briefly described and shown here as an example. All minerals groups have specific absorption features that vary as the specific composition of the mineral changes.

Spectroscopy and remote sensing are based upon the analysis of photons that have interacted with matter. Whereas thermal infrared data provides compositional information, it has another unique property not evident in other wavelength regions. All common rock-forming minerals have high absorption coefficients over the thermal infrared region that are a function of the mineral's index of refraction [Moersch and Christensen, 1995]. Therefore, there is very little to no volume scattering and the

photons detected have generally only interacted with one particle. This promotes the linear combination of TIR photons as multiple interactions are restricted. However, where particle sizes are reduced, volume scattering dominates and TIR data no longer adds linearly [Moersch and Christensen, 1995; Ramsey and Christensen, 1998] (Figure 8). The position of the absorption feature does not change, but the depth of the absorption does where particle sizes are decreased [Lyon, 1965] (Figure 8).

As TIR energy is emitted from all materials, atmospheric absorptions can occur. These depend upon the composition, thickness, and temperature of the atmosphere. On Earth, there is a clear (little to no atmospheric absorption) atmospheric window between the 8 – 12 μm region. Hence, this is the TIR spectral region used by ASTER, the Thermal Infrared Multispectral Scanner (TIMS), LandSat Thematic Mapper (TM), and various other TIR instruments that have observed Earth. However, stratospheric ozone (O_3) has an absorption band from 9.3 μm to 10.2 μm that affects data collected by spaceborne TIR instruments more significantly than that from airborne instruments. Whereas tropospheric ozone (a component of smog) is abundant in urban areas, the troposphere on surrounding Meteor Crater should not contain large amounts of O_3 .

2.2.1. Calculation of Emissivity

The separation of TIR radiant energy into temperature and emissivity is performed on all three (ASTER, TIMS, and THEMIS) TIR data sets used in this study and is described here for ASTER TIR data. The same methodology applied to the TIMS and THEMIS data processing as well.

Emissivity is defined as the ratio of the radiant energy of an object divided by the radiant energy of a blackbody at the same wavelength. By definition, a blackbody is a perfect absorber and emitter and has an emissivity of 1.000 at all wavelengths.

According to the Planck equation, the emitted radiant energy (E) of a blackbody at a specific wavelength (λ) is a function of the object's temperature (T) at that wavelength, or

$$E(\lambda, T) = \frac{2\pi hc^2}{\lambda^5 (e^{hc/\lambda kT} - 1)} \quad (1)$$

where h is Planck's constant, c is the speed of light, and k is Boltzmann's constant. The values of each constant are as follows:

$$\pi = 3.14159265356$$

$$h = 6.6260755 \times 10^{-34} \text{ J s}$$

$$c = 2.99792458 \times 10^8 \text{ m/s}$$

$$k = 1.380658 \times 10^{-23} \text{ J/K}$$

With multispectral TIR data, the temperature and emissivity of the pixel are not collected or calculated by the detector. The sole purpose of the detector is to collect and record TIR radiant energy over a specific number of wavelengths. In order to separate radiant energy into both temperature and emissivity, either the sole temperature or one of the emissivity values (one for each TIR band) must be assumed. The normalized emittance technique is chosen for this assumption. As described by *Realmuto* [1990], the maximum emissivity value is chosen, but the wavelength at which this emissivity occurs is not specified. *Salisbury and D'Aria* [1992] examined over 60 samples of a variety of compositions and found an average maximum emissivity value of 0.983 ± 0.002 . Due to

this and results from another study [*Ramsey and Fink, 1994*], a maximum emissivity value of 0.985 is used for the ASTER TIR and TIMS data used in this study.

2.2.2. Spectral Deconvolution Analysis

Deconvolution modeling is based upon the principle that a TIR spectrum is a linear combination of the individual constituent end-member spectra in proportion to the constituent's areal abundance. For example, the spectrum of a rock is a linear combination of the minerals composing that rock in proportion to the areal abundance of each mineral. Similarly, the spectrum of a remotely sensed pixel in a TIR image is a combination of the end-member spectra exposed on the surface.

Whereas the linearity of TIR spectra was assumed decades earlier [*Lyon, 1965*], the first attempt to quantitatively describe the limits of accuracy and particle size limits of spectral deconvolution was carried out by *Ramsey* [1996; *Ramsey and Christensen, 1998*]. In that study, the deconvolution of TIR spectra was found to be 94% accurate. Further, the limit below which the emissivity spectrum of a mineral ceases to add linearly was found to be $\sim 60 \mu\text{m}$. This agrees qualitatively with earlier studies that estimated this value to be $\sim 100 \mu\text{m}$ [*Salisbury and Walter, 1989; Moersch and Christensen, 1995*].

The deconvolution algorithm used in this study is summarized below and described in detail by *Ramsey and Christensen* [1998]. Its application to the TIMS TIR data of Meteor Crater is described by *Ramsey* [2002a]. At a specific wavelength (λ), the emissivity of a mixed spectrum (ϵ_{mix}) of η end-members is equal to the areal percentage (ζ) of each end-member times the emissivity of that end-member ($\epsilon(\lambda)$) with some residual error, $\delta(\lambda)$:

$$\varepsilon(\lambda)_{\text{mix}} = \sum_{i=1}^{\eta} \zeta_i \varepsilon(\lambda)_i + \delta(\lambda) \quad (2)$$

and all areal percentages must sum to 1 (or 100%), expressed as:

$$\sum_{i=1}^{\eta} \zeta_i = 1.000 \quad (3)$$

and residual error is calculated as:

$$\delta(\lambda) = \varepsilon(\lambda)_{\text{measured}} - \varepsilon(\lambda)_{\text{modeled}} \quad (4)$$

The residual error term, $\delta(\lambda)$, describes the difference between the model and measured emissivities and is used for calculating the root-mean-square (RMS) error. RMS error is a qualitative measure of how well the chosen end-members and their combined modeled emissivities fit the measured emissivity [Ramsey and Christensen, 1998]. The RMS error can be used to determine the better fit, with lower values indicating better fits. The RMS error with m bands is defined as:

$$\text{RMS} = \left[\sum_{i=1}^m \delta(\lambda)_i^2 / m \right]^{1/2} \quad (5)$$

2.3. Instrument Descriptions

2.3.1. The ASTER instrument

The Advanced Spaceborne Thermal Emission and Reflection Radiometer (ASTER) is a multispectral imager currently onboard the Terra satellite [Kahle *et al.*, 1991; Abrams, 2000]. Terra is part of NASA's Earth Observing System (EOS) program and includes scientists from the United States, Japan, France, and Australia. ASTER was

launched in December 1999 and was the first spaceborne multispectral (> 2 bands) TIR instrument. ASTER obtains daytime images at approximately 10:30 AM local time at the equator crossing.

ASTER contains 14 bands within three separate instrument subsystems. There are three bands in the visual to near infrared (VNIR) wavelengths from 0.52 μm to 0.86 μm , six bands in the short wave infrared (SWIR) wavelengths from 1.60 μm to 2.430 μm , and five bands in the TIR from 8.125 μm to 11.65 μm . Table 2 lists the ASTER instrument specifications as they appear in *Abrams* [2000]. Approximate filtered band centers for the five TIR bands are listed in Table 2 and TIR spectral response functions are shown as Figure 9. The instrument has a swath width of 60 km over the three wavelength regions and spatial resolutions of 15, 30, and 90 for the VNIR, SWIR, and TIR, respectively. The VNIR subsystem has both a nadir-looking telescope for the three bands listed on Table 2 and a backwards-looking telescope for the VNIR band at 0.8040 μm . This band is used in conjunction with Band 3 (0.76 μm – 0.86 μm , band center at 0.8070) to produce digital elevation models (DEM's). A DEM produced for Meteor Crater is shown as Figure 10.

ASTER TIR is the primary data used in this study, so the TIR subsystem is described as such from *Kahle et al.* [1991]. The TIR subsystem uses a Newtonian catadioptric system with an aspheric primary mirror. Unlike the telescopes used in the VNIR and SWIR subsystems, the telescope of the TIR subsystem is fixed with the pointing and scanning done by a mirror. Each band uses 10 Mercury-Cadmium-Tellurium (HgCdTe) detectors in a staggered array with optical bandpass filters (as listed

in Table 2). A mechanical split Stirling cooler is used for maintaining the detector temperature at 80 K.

2.3.2. The TIMS instrument

The Thermal Infrared Multispectral Scanner (TIMS) was the sole TIR instrument used in the earlier analysis of TIR data of Meteor Crater [Ramsey, 2002a]. Due to this and the fact that this study continues Ramsey's work, the TIMS is briefly described herein.

The TIMS instrument is a cross-track TIR imaging scanner with 6 bands between 8 μm and 12 μm . Table 3 lists the TIR channels of the TIMS instrument and their appropriate band center. TIMS is airborne, so the spatial resolution is a function of the aircraft height. The TIMS data used in this study has a spatial resolution of 3.2 m/ pixel. Because the TIMS data is of much higher spatial resolution than the spaceborne ASTER data over roughly the same region of TIR wavelengths, the TIMS is used as a basis of comparison for the ASTER TIR data.

2.3.3 The THEMIS instrument

The Thermal Emission Imaging System (THEMIS) is a multispectral TIR instrument on the Mars Odyssey spacecraft and is noted in the title of this work. THEMIS has TIR and VNIR subsystems that began to return images in February 2002. For the TIR subsystem, THEMIS has 9 channels from 6.5 μm to 14.5 μm and a tenth channel with a band center at 15 μm that aids in the calculation of atmospheric temperature [Christensen *et al.*, 1999a, 1999b]. Figure 11 displays the TIR spectral

response functions for THEMIS and Table 4 lists the band centers and band widths for the TIR and VNIR systems. The defining characteristic of THEMIS is its TIR spatial resolution of approximately 100 m. This is the highest spatial resolution of Mars in the TIR wavelengths. The specific objectives of the THEMIS experiment are summarized here because this work represents a preliminary examination of THEMIS TIR data and future work may constrain these objectives. The primary objectives and science goals of THEMIS are to determine the mineralogy and petrology of the surface of Mars utilizing the hyperspectral data of the Mars Global Surveyor (MGS) Thermal Emission Spectrometer (TES) in order to study small-scale geologic processes and potential future landing sites with the focus being potential sites of hydrothermal or sub-aqueous environments [Christensen *et al.*, 1999a, 1999b]. Whereas the Thermal Emission Spectrometer (TES) is a hyperspectral TIR instrument with a spatial resolution of 3.15 km, THEMIS will map Mars with just nine bands, but with a 900% increase in spatial resolution. It has been demonstrated that nine TIR spectral bands in the spectral region of THEMIS is sufficient to identify mineral classes at abundances of ~10% [Feely and Christensen, 1999]. Carbonates, silicates, sulfates, phosphates, hydroxides, and oxides have strong absorptions in the 6.5 μm to 14.5 μm region.

THEMIS has five bands in the VNIR from 0.425 to 0.860 microns and a spatial resolution of 18 m. This provides another high-resolution tool to complement the Mars Orbital Camera (MOC) on the MGS spacecraft to image ejecta blocks, crater walls, and crater gullies.

2.4. Thermal Infrared Remote Sensing

2.4.1 Earth

Due to its unique characteristics as described above, TIR remote sensing has been used to address various geologic problems on Earth such as geologic mapping, sediment transport, source lithologies, and monitoring of active volcanoes [*Hook et al.*, 1994; *Ramsey et al.*, 1999; *Bandfield et al.*, 2002; *Ramsey and Fink*, 1999, respectively]. Remote sensing is useful if the region under investigation is too large, dangerous, or inaccessible enough to warrant fieldwork. Further, remote sensing on Earth and subsequent ground-truthing is useful to apply to analogous surfaces of planets where fieldwork is not possible. An example is this study of Meteor Crater.

2.4.2 Terrestrial Analogs and Instrumental Proxies

Due to their similar spatial and spectral resolutions, it has been suggested that ASTER be a proxy for THEMIS [*Ramsey*, 2002b, 2002c] and previous studies have done so [*Hellman and Ramsey*, 2003]. Meteor Crater has been used in the past as a terrestrial analog for extraterrestrial impact craters [*Garvin et al.*, 1988; *Grant and Schultz*, 1993]. For example, Meteor Crater is used for interpreting the effects of erosion on Mars [*Grant and Schultz*, 1992, 1993] and Magellan radar data on Venus [*Garvin et al.*, 1989].

2.4.3 Mars

Various thermal infrared instruments have flown aboard spacecraft that have visited Mars since 1969 and have contributed to our knowledge of the composition of Mars [ref. – the surface composition chapter of *Mars*]. Before this, ground-based

telescopic TIR measurements were analyzed [*Van Tassel and Salisbury, 1964; Sinton, 1967*].

The first TIR instruments to return data from Mars include the Infrared Spectrometer (IRS) and the Infrared Radiometer (IRR) on Mariners 6 and 7, the Infrared Interferometer Spectrometer (IRIS) and an IRR on Mariner 9, and the Viking Infrared Thermal Mapper (IRTM) on both Viking spacecraft [*Hanel et al., 1972a, 1972b; Kieffer et al., 1977*].

The IRS and IRIS were hyperspectral TIR instruments, but had low spatial resolutions of approximately 150 km and >110 km, respectively. For these instruments, studying the martian atmosphere, and not the surface composition, was the main objective [*Hanel et al., 1972a; 1972b*]. All three IRR instruments had two broadband thermal channels at 10 μm and 20 μm with a spatial resolution of about 50 km on Mariners 6 and 7 and 15-100 km on Mariner 9. The data were useful for analysis of thermophysical properties of the martian surface, but not compositional information [*Kieffer et al., 1973*].

The Viking IRTM was designed to map the thermophysical properties of the martian surface [*Kieffer et al., 1972*]. The IRTM had a higher spatial resolution (>30 km) than previous instruments and was multispectral, with five broadband channels centered at 7, 9, 11, 15, and 20 μm . Absorption bands were observed in the 9 and 20 μm spectral regions over low albedo regions [*Kieffer et al., 1977; Christensen, 1982, 1998*] that are consistent with sand-sized basaltic surfaces [*Bandfield, 2002*]. Atmospheric subtraction and determination of surface composition was difficult due to the IRTM's limited spectral resolution [*Christensen, 1998*].

The Termoskan instrument was a radiometer aboard the Soviet Union's Phobos 1988 mission and collected TIR data in one broadband channel from 8.5 to 12.0 μm over random areas of Mars. Termoskan data have been analyzed in conjunction with martian impact craters [*Betts and Murray, 1993*], and hence is discussed in section 2.5.

More recently, the Thermal Emission Spectrometer (TES) on the Mars Global Surveyor (MGS) and the Thermal Emission Imaging System (THEMIS) aboard Mars Odyssey have imaged Mars with the highest spectral (TES) and spatial (THEMIS) resolutions to date in the TIR wavelengths. The spatial and spectral resolutions of the U.S. TIR instruments discussed here are compared in Table 1.

TES is a hyperspectral spectrometer that has returned TIR data of the martian surface and atmosphere over 143 bands from 5.8 – 50 μm [*Christensen et al., 1992, 2001*]. With its increased spatial and spectral resolution over previous martian TIR instruments, TES has been used to determine the distributions of minerals [*Bandfield et al., 2000; Bandfield, 2002*] and igneous lithologies [*Christensen et al., 2000a; Rogers and Christensen, 2003*] in the low-albedo regions and the extent of the global dust cover [*Ruff and Christensen, 2002*].

For all compositional studies involving the TES instrument, only those of the low albedo regions have been determined [*Bandfield et al., 2000; Christensen et al., 2000a, 2000b; Bandfield, 2002; Rogers and Christensen, 2003*]. Due to particles < 60 μm (such as dust) scattering TIR energy, the composition of the dust and underlying bedrock of the high albedo, dusty regions on Mars has not been determined using TES data. It is hoped that this study will introduce techniques that can be performed with high resolution, multispectral TIR data (such as THEMIS) of fresh impact craters in the high albedo

regions. The composition of the underlying lithologies may provide insight into the geologic history of the high albedo regions.

THEMIS has been mapping the martian surface since February of 2002 [*Christensen et al.*, 2002, 2003a, 2003b]. The instrument characteristics and scientific objectives of THEMIS are discussed in section 2.5.3.

2.4.4. Use of image end-members

The use of image end-members in deconvolving multispectral TIR data is well described by *Ramsey* [2002a]. A summary of the benefits of using image end-members over vast spectral mineral libraries is discussed here.

The first reason is the limits of the deconvolution algorithm. For an accurate deconvolution, there can only be as many end-members as the number of bands [*Ramsey and Christensen*, 1998]. For hyperspectral data such as TES, this limit of the number of end-members is not a significant factor. However, multispectral data sets such as ASTER or THEMIS only contain 5 to 10 channels. Hence, ASTER TIR data can be accurately deconvolved with only 5 or less end-members and THEMIS TIR with 9 or less.

For multispectral TIR data sets, deconvolving with laboratory mineral spectral libraries generally poses problems in interpretation. Outcrops and ejecta blocks consist of specific lithologies, and these lithologies may share common minerals, but contain varying amounts of these as well as unshared minerals. A second reason is the large size associated with mineral spectral libraries compared with the multispectral data and the knowledge of the remotely-sensed area. Whereas at least 60 to 70 common rock-forming

minerals should be included in a mineral spectral library (e.g., [Bandfield, 2002]), the multispectral data set only has 5 to 10 bands at which TIR radiance is collected and filtered. A geologic scene typically only contains ~5 distinct minerals [Gillepsie *et al.*, 1990], but an improper spectral library in incorrect proportions may “fit” the TIR spectra and appear to be correct if the RMS errors of multiple deconvolution models are not critically compared. However, by definition, image end-members are contained within the data collected over the area.

The conditions, characteristics, spatial resolution, and spectral resolution of the laboratory spectrometer and the multispectral TIR remote sensing instrument seldom agree. For example, laboratory TIR spectra generally have a spatial resolution of 1 cm whereas ASTER TIR and THEMIS TIR operate over 90-100 m spatial resolution. Further, separating the TIR radiance of the surface and atmosphere should not significantly affect the results of the image end-member analysis. Nearby (at the scale of an ejecta blanket of a small impact crater) pixels at the same surface elevation in the same multispectral TIR scene should have approximately similar amounts of contribution from the atmosphere. Whereas the spectra of the pixels are affected by atmospheric absorptions, the distribution of those pixels is not. The distribution of end-members will closely reflect the distribution of end-members on the surface. This is comparable to the ratio of emissivity spectra of nearby TES pixels to discern surface features without atmospheric separation [Ruff and Christensen, 2002].

2.5. Impact Craters on Mars

Martian impact craters and their various properties have been studied in detail since the earliest days of Mars science [Leighton, 1967; Masursky, 1973; Carr, 1981]. However, these studies have primarily focused on the larger impact structures such as central peak craters and multi-ring basins. Simple impact craters are defined as those in which the pressure associated with impact are not high enough to produce the isostatic rebound needed for a central peak and rings to form [Melosh, 1989]. Generally, simple impact craters are bowl-shaped [Melosh, 1989]. Ejecta studies have focused on rampart and lobate ejecta blankets. With Viking data, 42,283 impact craters with diameters larger than 5 km have been catalogued [Barlow, 2000] and the youngest of these have been noted. Small, simple impact sites have not been studied in detail due to the low spatial resolution of orbital cameras [Carr, 1981]. For similar reasons, these structures have never been imaged or studied with TIR instruments before the advent of THEMIS.

Small, simple, bowl-shaped craters have only been studied in detail with the Mars Orbital Laser Altimeter (MOLA) instrument [Garvin *et al.*, 1999, 2000, 2003]. The studies are geometric and are subject to whether or not the crater was directly sampled by the laser altimeter. A depth (d) to diameter (D) ratio of $d = 0.21D^{0.81}$ for martian simple (<7 km diameter) craters was the result of the ongoing study.

The only study of martian impact craters and their associated ejecta blankets performed with the aid of TIR remote sensing was done with the Phobos '88 Termoskan instrument [Betts and Murray, 1993]. One hundred and ten impact craters on the plains near Vallis Marineris with diameters between 4.2 km and 90.6 km were examined with one broadband TIR channel (8.5 – 12 μm) and a spatial resolution of 1.8 km. The work described Ejecta blankets Distinct In the THERmal infrared (EDITHs) as ejecta blankets

that have a higher or lower radiance than the surrounding terrain. The reason is attributed to Hesperian units being more thermally distinct than the older Noachian or younger Amazonian units. The degree of erosion and the local availability of eolian material is noted as a secondary cause of EDITHs. This work will argue that the thermal inertia influenced by the particle size, preservation, and mantling of the ejecta blanket are the causes of EDITHs and not the relative geologic age (e.g., Noachian or Hesperian) of the surface.

Early analyses of THEMIS results have found the ejecta blankets of impact craters to have varying thermophysical properties that *Christensen et al.* [2002, 2003a, 2003b] attributes to the age of the impact and not the geologic age of the surface. This work will agree with and further their conclusion concerning the thermal infrared signature of crater ejecta.

2.5.1. Geology of a small impact site in Syrtis Major Planum

The THEMIS instrument imaged a small impact crater in Syrtis Major on two occasions with the TIR subsystem. The crater is located in southwest Syrtis Major in the southern highlands at approximately 4° S, 59° E (Figure 12). THEMIS VNIR data of the crater have either not been collected or released, and orbital data from various instruments on the Mars Global Surveyor (MGS) could not be acquired or are not available. This includes data from the Mars Orbital Camera (MOC), Mars Orbital Laser Altimeter (MOLA) and the Thermal Emission Spectrometer (TES). TIR data from the TES, Viking IRTM, and all Mariner IRS and IRR instruments have spatial resolutions that are too low to accurately image the crater, which has a rim to rim diameter of

approximate 1.1 ± 0.1 km, based upon the THEMIS TIR spatial resolution of 100 m.

Measurements of the diameter and other crater properties can be accurately constrained where THEMIS VNIR, MOC, or other high-resolution data are acquired of the area.

The Syrtis region is abundantly cratered and has an overall low albedo of 0.12 [Ruff and Christensen, 2002]. Previous studies of thermal inertia have found the low albedo regions of Mars to be composed of coarse-grained particles (200–500 μm in diameter) [Palluconi and Kieffer, 1981]. Deconvolution of TES spectra have suggested calcium pyroxene and plagioclase to be the dominant minerals of the Syrtis region [Bandfield et al., 2000; Bandfield, 2002]. Other studies using the Phobos ISM data find low-calcium pyroxene in the Syrtis Major region [Mustard et al., 1993]. Each of these previous studies agree that Syrtis Major is composed of basalt and basaltic sediments.

The reasons for selection of this particular crater in Syrtis Major are fourfold. First, the crater is approximately the same size as Meteor Crater (from analysis and measurement of TIR images). Second, there exists both daytime TIR and nighttime TIR data of the crater, and it is believed that this will be useful in showing differences in the thermal inertia of the ejecta blanket versus that of the surrounding plain. The third reason the crater was chosen is that if the differences in particle sizes between the rim and ejecta versus the surrounding plain are apparent in this low-albedo region, this algorithm and methodology should apply to high-albedo regions. Fourth, the particle size and composition of the Syrtis Major region is well-known from previous studies [Mustard et al., 1993; Bandfield et al., 2000; Bandfield, 2002] and this provides a means of comparison to the THEMIS TIR data used in this study.

The THEMIS TIR daytime scene (I01297001) of the aforementioned crater was acquired on 31 March 2002. Martian craters with diameters less than 5 km are unnamed [Barlow, 2000]. Viking topography data of southwest Syrtis Major and the location of the scene are shown in Figure 12. For this scene, all ten bands were released to the public (Table 4). The radiance data of band 3 (band center at 7.93 μm) of scene I01297001 of the crater and surrounding plain is shown as Figure 13. The image is 320 pixels, or approximately 32 km, across. The continuous ejecta blanket (CEB) and the ejecta rays appear to have a lower radiance than the surrounding plain in all TIR wavelengths.

The nighttime THEMIS TIR scene (I01852006) of the crater was acquired on 16 May 2002 (Figure 15). TIR bands 4, 9, and 10 were released to the public. Of these, only bands 4 and 9 are useful for surface radiance. Part of the CEB is not imaged in the nighttime scene. For both nighttime radiance bands, the CEB of the crater has a higher radiance than the surrounding terrain. This property of the CEB and its relation to particle size is discussed in detail in section 4.

Figure 14 displays Viking topography data and the coverage of nighttime THEMIS image. In both TIR scenes, the extent of the CEB varies from 1.7 to 5.1 km around the crater rim. Rays are apparent in the far-field ejecta blanket, indicating a young impact age [Melosh, 1989]. According to the Mars Crater Morphology Consortium [Barlow *et al.*, 2000], this particular crater should be described as fresh, “dry”, and rayed. “Dry” indicates that the crater ejecta were not fluidized and therefore not associated with “splish” craters or near-surface volatiles [Barlow *et al.*, 2000].

3. Methodology

3.1 Acquisition and Processing of ASTER TIR Data

ASTER data products are acquired from the Distributed Active Archive Center maintained by United States Geological Survey (USGS) Earth Observing System (EOS) Data Gateway. The ASTER data of Meteor Crater were acquired at 18:22:22 UTC on 16 September 2002. Raw uncalibrated data are referred to as Level 1A and are in digital numbers (DN's) that represent the radiance at sensor. Raw data that have been radiometrically and geometrically corrected are referred to as Level 1B data, and are not atmospherically corrected (Figure 16).

The Level 1B scene was atmospherically corrected with the data representing radiance at surface in DN's. Designated as a Level 2 product, the data are converted to radiance at surface in the units of $W/m^2/sr/\mu m$ through accompanying band scale factors. These radiance data are separated into temperature and emissivity for the purposes of this study. This calculation is discussed in section 2.2.1 and applies to all TIR data (ASTER, TIMS, and THEMIS).

Table 5 lists the ASTER granule ID's of the Level 1A, Level 1B, and Level 2 images used for this study. Although both temperature and emissivity data are available through USGS EOS Data Gateway, only TIR radiance data are acquired and analyzed for the purposes of this study. In this, ASTER TIR radiance data represents a proxy for THEMIS TIR radiance data.

3.2 Selection of ASTER TIR Image End-Members

Spectral Mapping Wizard, a subprogram in the ENVI software program, was used to group each pixel in the ASTER TIR emissivity scene. A 5-dimensional plot is created with each dimension representing a band of the emissivity image. Each pixel, containing

5 dimensions of data, is placed in the 5-dimensional space and a cluster of data is the result (Figure 17). Pixels that are the most spectrally distinct lie at the ends of the cluster and are selected as image end-members. For the ASTER TIR scene of Meteor Crater, the spectra of the three most spectrally distinct pixels are displayed as Figure 18. The ASTER TIR emissivity image will be deconvolved with the three selected image end-members. As described in section 2.3.4., these image end-members obviously have identical wavelengths as the original ASTER emissivity data. Spectral responses or filter functions do not need to be applied.

The image end-members are labeled as IEM1, IEM2, and IEM3, and are represented as spectral data and not specific lithologic spectra. The spectral characteristics of the image end-members reveal their compositional properties. Comparison with the ASTER sample end-member analysis and the high-resolution TIRS end-member analysis will yield conclusions about the composition of each ASTER image end-member. This is discussed in section 4.

The image end-members of the TIRS and THEMIS scenes are chosen by identical means. However, the number of bands and hence the number of dimensions of the scatter plot generated will depend upon the TIR data set.

3.3 Sample Collection and Emission Spectra of Meteor Crater Lithologies

Field work was performed at Meteor Crater from 27 July 2002 to 30 July 2002. Samples of each lithology were collected and the location of each sample collection site was recorded with a Trimble differential Global Positioning System (GPS) Pathfinder Pro

XRS unit. It should be noted that samples consisted primarily of the weathered tops of outcrops and local fresh surfaces.

The areal extent of local lobes in the ejecta blanket were recorded with the GPS unit. Coconino ejecta lobes on the eastern near-field ejecta blanket and Kaibab ejecta lobes on the northern far-field ejecta blanket were the primary targets. Additionally, the northeastern, far-field ejecta blanket was analyzed. The earlier TIMS image end-member analysis [Ramsey, 2002a] showed this area to be abundant in Coconino Sandstone. This is significant because the erosion of the ejecta at Meteor Crater was estimated to be either 20-30 meters [Shoemaker, 1960; Roddy, 1978] or just 1-2 meters [Grant and Schultz, 1993; Ramsey, 2002a]. The amount of Coconino Sandstone present affects any calculation of the amount of erosion that has taken place.

A Nicolet Nexus 670 spectrometer with a deuterated triglycine sulfate detector at Arizona State University was used to acquire thermal emission spectra (as described by [Ruff *et al.*, 1997; Johnson *et al.*, 2002a, 2002b]) of the rock samples of the lithologies at Meteor Crater. Rock samples were heated to 80° C in an oven and then placed in a nitrogen-purged glovebox during spectral acquisition. Radiant energy was collected by a parabolic mirror and directed toward the interferometer. One hundred and twenty scans of the radiance from ~5 to 50 μm were measured, averaged, and stored. The temperature of the sample was not kept constant during data acquisition. However, this anisothermality has been shown to be insignificant in collecting thermal emission spectra [Bandfield *et al.*, 2002]. Two blackbodies (at 70° C and 100° C) were used for radiometric calibration of the spectrometer and for removal of the energy emitted by the instrument and surrounding room.

To convert to emissivity, a software program incorporated instrument temperature, the two blackbody spectra, and divided each sample's radiance spectrum by the Planck blackbody radiance spectrum calculated for the maximum brightness temperature. It was assumed that the spectrum has an emissivity equal to 1.000 at the maximum brightness temperature [Ruff *et al.*, 1997].

There are slight differences in the laboratory emission spectra of the weathered tops of samples and spectra of the fresh bedrock. It was decided to use the emission spectra of the weathered tops of each lithology as sample end-members because this is what is observed by the spaceborne TIR detector.

Figure 19a displays the sample spectra of the Meteor Crater lithologies as obtained by the spectrometer. Although TIR data was acquired from ~5 to 50 μm , only the region of wavelengths observed by the ASTER and TIMS instruments are shown. The absorption band of quartz / silica (SiO_2) is evident in the Coconino Sandstone spectrum. The Kaibab Formation spectrum is spectrally flat over the wavelengths used in this study. The Moenkopi Formation, which has local silica and clay.

With the same lithologic color scheme as Figure 19a, Figure 19b displays the laboratory spectra convolved with ASTER TIR spectral response functions to simulate how ASTER would observe each pure lithology with no other lithologies or contaminants present. Whereas the lithologies are still distinct, they have lost some spectral character due to the filtering from 198-point spectra to 5-point spectra. These filtered spectra are now considered the sample end-member spectral library.

3.4 Linear Spectral Deconvolution

The ASTER TIR image of Meteor Crater was deconvolved using the algorithm developed by Ramsey [1996; Ramsey and Christensen, 1998]. The algorithm (described in section 2.2.2 of this work) was input into an IDL subprogram of the ENVI software program. Two separate trials were performed, using both three image end-members and three sample end-members on the other. The deconvolution results, comparison of the two, and the RMS errors associated with each are discussed in section 4. Figure 18 and Figure 19b show the image end-member spectra and sample end-member spectra, respectively. Figures 20 and 21 display the image end-member analysis and sample end-member analysis, respectively. These are discussed in the next section.

3.5. Acquisition and Processing of TIMS TIR Data

TIMS TIR data of Meteor Crater were acquired at 1230 LT on 22 August 1994. The TIMS instrument was scanning on a NASA C-130 aircraft that had an elevation of 1219 m above ground level. This resulted in a spatial resolution of 3.2 m/pixel. The image is 1420 pixels by 630 pixels and contains the entire crater, ~1 km west of the crater, and ~3 km east of the crater. There is very little data north and south of the crater. The radiance data are in units of $\text{mW}/\text{m}^2/\text{sr}/\mu\text{m}$. Similar to the ASTER TIR data, ENVI is used to calculate emissivity for each pixel and produce a separate image file. A maximum emissivity of 0.985 was used for the separation of emissivity and temperature, similar to the results of earlier studies [Salisbury and D'Aria, 1992; Ramsey and Fink, 1994]. The TIMS data represent high spatial resolution TIR data that can be used to assess the validity and accuracy of the ASTER TIR data, and were validated using field observations.

3.5.1 Selection of TIMS TIR image end-members

The TIMS TIR data used in this study are identical to those used by *Ramsey* [2002a] in an earlier TIMS TIR image end-member analysis. In that study, image end-members were selected based upon knowledge of the location and spectral character of specific outcrops and pixels, respectively. In this study, the most spectrally distinct pixels are chosen to be image end-members by the image processing software algorithm. This is identical to the methodology to which the ASTER image end-members were chosen. The TIMS image end-members are shown as Figure 23.

3.6. Description of Regions of Investigation

Various sites were chosen in and around Meteor Crater are identified and compared on the low-resolution (90 m) ASTER and high-resolution (3.2 m) TIMS end-member analyses. Specifically, the areal abundances of end-members in certain areas will be compared to determine the change in accuracy where Meteor Crater is examined with a 790% decrease in spatial resolution. The regions where the areal abundance of Coconino Sandstone is investigated is significant for detection of lithologies on Mars with THEMIS TIR data. Meteor Crater provides a unique impact site where the area's surface exposure of one lithology is solely due to meteorite impact. The Coconino Sandstone would not be evident in the inner crater walls, floor talus, rim, and ejecta if impact had not occurred. The lithology is not exposed anywhere else in this area of the Canyon Diablo region (Figure 1). Whereas sandstones have not been detected on Mars [*Bandfield et al.*, 2000; *Bandfield*, 2002], investigations of the areal extent of Coconino

ejecta at Meteor Crater serve as analogs for the examination of ejected lithologies on Mars. This has implications for determining estimates of pre-impact stratigraphy (lithologies and their thicknesses) on Mars with THEMIS TIR data of fresh impact sites.

These regions of investigation at Meteor Crater include:

- 1) the extent of the northeastern windstreak
- 2) the identification of one major and three minor zones in the windstreak
- 3) the areal abundance of the strata and debris aprons of Coconino on the eastern inner-crater wall.
- 4) areal amount of Coconino Sandstone
- 5) areal amount of Moenkopi Formation
- 6) The difference in areal abundances in using sample emission spectra as end-members as opposed to image end-member spectra.

Items 1-4 involve specific investigations of the areal abundance of the Coconino Sandstone. This is significant for the above reasons and because the composition, and therefore the thermal infrared spectra, of the Coconino Sandstone composing the windstreak is very distinct from that of the other two lithologies. Further, as shown at Meteor Crater, the mineralogic and lithologic character of windstreaks on martian impact craters may be the only location that reveals information about ejected lithologies. It is necessary to investigate this property of the ASTER data to determine its likelihood for THEMIS data. For similar reasons as those given for investigating the windstreak, it is necessary to investigate this to determine what THEMIS TIR data will reveal about inner-crater strata on Mars.

Item #5 involves testing the limits of deconvolving ASTER TIR data to identify lithologies with low areal abundances. Because the distribution of Moenkopi Formation is accurately identified by analysis of TIMS data, this can be used to compare with ASTER data of the same region. The total areal percentage of the Moenkopi Fm. end-member in a selected region is compared for each end-member analysis.

Item #6 is discussed in section 4.3.1 and is a comparison of areal abundances of each end-member from the two ASTER end-member analyses. The areal abundances of each end-member at three different scales are compared.

3.7. Acquisition and Processing of THEMIS TIR Data

The THEMIS science team is required to release a portion of THEMIS data to the public quarterly each year. The first such release occurred 1 October 2002 and will continue during the primary mission phase. VNIR and TIR data are available on the THEMIS web site at <http://themis.asu.edu>. TIR data exists in two forms. There exists raw radiance data (Experimental Data Record – EDR) and calibrated radiance data (Reduced Data Record – RDR). Calibrated data (RDR) describes raw radiance data (EDR) that have been calibrated to remove instrument errors and better represent the actual radiance at sensor. The IR-RDR data are given in integer format, with scaling factors given to convert to floating point format. Using the conversion will result in floating point numbers that represent radiance in units of $W/cm^2/sr/\mu m$. TIR data corresponding to daytime and nighttime are released. Daytime (odd-numbered orbits of the Odyssey spacecraft) TIR data consists of 10 bands whereas nighttime (even-numbered orbits of the Odyssey spacecraft) consists of 3 – Bands 4, 9, and 10.

The THEMIS TIR data are not geometrically corrected and show obvious band to band misalignment. This is due to the side-by-side alignment of the TIR detectors and the movement of the Odyssey spacecraft as radiance is detected. A simple, crude geometric correction was applied by observing and recording the pixel location of a specific surface feature as it changed from band to band. The geometric offset from band to band was calculated, and the corresponding number of samples and lines were deleted from the image edges. This qualitative correction lessened the geometric distortion from band to band, but did not entirely eliminate it. Because the spatial resolution of each pixel is 100 m, the geometric distortion was decreased to less than 100 m. A precise geometric correction is recommended for eliminating all geometric distortion.

As discussed under Instrument Descriptions (section 2.5.3), the THEMIS instrument has ten bands in the TIR region, but this study will use seven wavelength regions. Band 10, with a band center at 14.88 μm , is not useful for information about the surface [*Christensen et al*, 1999]. Carbon dioxide in the martian atmosphere absorbs TIR energy in this wavelength region [*Ruff and Christensen*, 2002]. Also, Bands 1 and 2, with identical spectral coverage and band centers at 6.78 μm , are ignored in this study. These two bands were designed to be averaged together to increase accuracy and increase signal to noise ratio (SNR), but early studies have found that these two have not been calibrated correctly [ref!!!!]. Ignoring the TIR data from bands 1, 2, and 10 leaves a 7-point TIR spectra for each pixel in the THEMIS scene. These spectra will not be atmospherically corrected, but it is believed that this will not significantly affect the results of an image end-member analysis (section 2.3.4.).

The radiance data were separated into temperature and emissivity using ENVI software. A maximum emissivity value of 0.99 was chosen from a Mars Dust Cover Index [Ruff and Christensen, 2002]. The emissivity data of the daytime scene are used to select image end-members as described in section 3.8. The daytime temperature, nighttime temperature, and daytime emissivity data of the crater are discussed in section 4.4.

3.8. Selection of THEMIS TIR image end-members

The purpose of this work is to use ASTER TIR data as a proxy for THEMIS TIR. Therefore, THEMIS TIR image end-members are selected using the same methodology as the image end-members of the ASTER TIR scene of Meteor Crater are selected. The radiance data are separated into emissivity and temperature data using the same process used for ASTER TIR and TIMS data. Whereas the nighttime temperature data proved to be useful in the determination of thermophysical properties of the crater, the nighttime emissivity data did not due to the limited data released (two bands excluding Band 10). Selection of image end-members and subsequent deconvolution of the image end-members would not provide for a useful analysis with this limited spectral resolution. The daytime emissivity scene consists of seven bands (Bands 3 – 9), and these data were used for selection and deconvolution of image end-members.

The Spectral Mapping Wizard function in the ENVI image processing software program is used to select the pixels within the daytime emissivity data that are the most spectrally distinct. This methodology is identical to that used for ASTER and TIMS data. The spectra of these pixels are selected to be the image end-members of the emissivity

scene and are displayed as Figure 24. Refer to Figure 11 for the spectral response functions of THEMIS and Table 4 for a listing of the THEMIS TIR band centers. Possibilities of the composition of the image end-members are discussed in section 4.4.2. A precise determination of the mineralogies composing the image end-members is beyond the scope of this work because atmospheric subtraction was not performed. Rather, the distribution of each image end-member will be investigated and discussed. The temperature data (4.4.1.), daytime emissivity data (4.4.2.), and the image end-member analysis (4.4.2) are discussed in section 4.4.

4. Results

4.1 ASTER TIR end-member analyses

4.1.1 Image end-member analysis and RMS error

The ASTER TIR emissivity scene of Meteor Crater is deconvolved using the image end-member library consisting of the 3 spectra shown in Figure 18. As noted in section 3.2, the spectra appear to correlate with the three lithologies found at Meteor Crater, but will be denoted as image end-member #1 (IEM1), IEM2, and IEM3 because these spectra were selected by the spectral distinctness and not by a priori knowledge of the image spectra or the lithologies at Meteor Crater.

The results of the image end-member analysis are shown as Figure 20a. The color scheme is based as follows for the 8-bit pixels: the percentage of each end-member from 0% to 100% is scaled as a digital number (DN) from 0 – 255. A DN of 255 correlates to 100% and a DN of 0 is 0% of that end-member. As per the deconvolution algorithm, two or more end-members cannot both be at or near 100%. The sum of the

areal percentages of the 3 end-members is at or near 100% even if one or two of these have an areal abundance of 0%. Ideally, the total would always be 100% for each pixel. However, due to the best fit of the spectra locally being a little less, the RMS error will increase.

For visual purposes, the data representing the areal percentages of each end-member from Figure 20a are stretched 1%, therefore 0 – 255 DN's represents areal percentages of 1% - 99% (Figure 20b). It should be noted that this stretch does not alter the data (i.e., the areal percentages) of any pixel. It simply affects the color scheme to better identify the areal distribution of each end-member.

The RMS error image is shown as Figure 25 with 0.000 (0.0%) correlating to 0 DN and 0.005 (0.5%) and above correlating to 255 DN. This image has been stretched 1% for visual enhancement of the 0.000 - 0.005 range of RMS errors. The majority of the pixels have a RMS error of 0.002 (0.2%) or less (as shown by the dark gray to black hue of the bulk of the pixels). This signifies that there is a difference of 0.0% to 0.2% between the measured emissivity of those pixels and the model fit of the three image end-members. The greatest RMS errors occur in a specific area east of the crater, on the crater floor, and to the southwest of the crater. The area high in RMS errors (as compared to the rest of the scene) that is east of the crater is the small (300 m diameter) farm that is abundant in green vegetation (Figure 2). No combination of the image end-members fit the TIR spectra of this region well. Inside the crater, Quaternary alluvium and talus dominates the floor. Whereas the spectra of Image End Member #2 (IEM#2) fits the spectra of the crater floor well, there is still local residual error. This can be

attributed to the abundance of both desert vegetation and local deposits (from the crater's Quaternary period as a post-impact lake) that resemble the IEM#2 spectral signature.

4.1.2. Sample end-member analysis and RMS error

The same ASTER TIR emissivity scene of Meteor Crater deconvolved with image end-members is also deconvolved with the sample end-member library. Recall that the three end-members are laboratory emission spectra that are convolved to the ASTER TIR spectral response functions (Figure 19b).

The results of the sample end-member analysis are shown as Figure 21a using the color scheme of the sample end-member spectral plots from Figure 19b: red is the Coconino Ss., green is the Kaibab Fm., and blue is the Moenkopi Fm. The DN's of each color from 0 – 255 are scaled to and represent the areal percentage of each lithology from 0% to 100%. The Moenkopi Fm., which is represented by blue, is noticeably absent from the sample end-member analysis. Every pixel in the scene contains a value of 0.000 for the Moenkopi sample end-member as it was ejected from the deconvolution algorithm due to a poor spectral fit. In this, the sample end-member analysis becomes a two-component, rather than three-component, solution. The best fit of each pixel is comprised of solely Coconino Ss. and the Kaibab Fm.

The sample end-member analysis is stretched 1% in Figure 21b for identification of the two end-members. The windstreak to the northeast is obviously composed of Coconino Ss. (red) and the remaining pixels in the scene contain either Kaibab Fm. or a combination of Coconino and Kaibab.

The RMS error image of the sample end-member deconvolution is shown as Figure 26. The range of DN's (0-255) represents RMS errors from 0.020 to 0.025 (2.0% to 2.5%). These RMS errors are an order of magnitude higher than the RMS errors associated with the image end-member analysis and represent a poorer fit to the ASTER data than that of the fit of the image end-members. The best fit (as evidenced by the darkest pixels in Figure 26) is the rim of the crater. This is significant because large particle sizes (boulders, pebbles) are abundant at the rim, and this is what was chosen to be sample end-member for the purpose of this study.

4.2 TIMS TIR image end-member analysis and RMS error

As discussed in section 3, the high-resolution TIMS TIR image end-member analysis is used to validate the ASTER TIR end-member analyses. The reasons are threefold. Field mapping using a Global Positioning System (GPS) unit provided ground-truth of the image end-member analysis created by *Ramsey* [2002a]. It was decided that the TIMS image end-member analysis was very accurate where the extent of ejecta lobes and inner-crater strata debris aprons were compared with the boundaries of end-members on the image end-member analysis image (Figure 26). At 3.2 m/pixel, the spatial resolution represents an increase of 791% over the 90 m spatial resolution of ASTER. Further, the spectral resolution of the TIMS instrument is slightly better than that of ASTER. As described in section 2, the TIMS has six TIR bands, including the acquisition of TIR radiance data over the ozone absorption band that ASTER cannot.

The emissivity image created using the TIMS data was deconvolved using the three TIMS image end-member spectra (as seen as spectral plot in Figure 23). As

discussed in section 3.5.1., image end-members were chosen based on the selection of the most spectrally distinct pixels by a software algorithm. Spectral plots of the TIMS image end-members are shown as Figure 23. Figure 28 is the TIMS image end-member deconvolution and Figure 29 is the RMS error image.

The TIMS image end-member deconvolution is nearly identical to the earlier one by *Ramsey* [2002a]. This demonstrates that image end-members were correctly chosen in that earlier study. For the purposes of this study, it was necessary to select image end-members with the same methodology as those selected for the lower-resolution ASTER and THEMIS data sets.

The RMS error values (Figure 29) range from 0.000 to 0.010. The regions that exhibit the highest RMS errors on the TIMS image end-member analysis are portions of the windstreak, the crater floor, and the farm 3 km east of the crater. The windstreak is clearly composed of the Coconino image end-member, but slight differences in the spectra of these pixels and the spectra of the image end-member promote a higher RMS error. These slight differences are most likely due to the effects of shock metamorphism, the variability of the local vegetation, and/or the patchiness from erosion on those portions of the windstreak. The crater floor exhibits a high RMS error as it is covered by sparse vegetation, lake sediments, Quarternary alluvium, and basaltic dust from the nearby San Francisco volcanic field. As these materials have spectra that is most similar to that of the Kaibab Formation, this end-member is chosen to represent a majority of the areal abundance of the crater floor. However, slight differences in these pixels' spectra promotes a higher RMS error. The farm has abundance green vegetation which cannot

be modeled correctly by any of the three end-members. Due to this, high RMS errors are apparent for the pixels representing the farm.

4.3 Discussion

4.3.1. Comparison of ASTER end-member analyses

The ASTER end-member analyses were deconvolved with two different 3-end-member sets. Hence, the results of each vary from one another. Here, certain aspects of the differences between the two are discussed and potential reasons are given. The end-member deconvolution are compared on three scales:

- 1) the entire image that was deconvolved, or 90 pixels (8.1 km) on each side (as seen in Figures 20 and 21)
- 2) just the CEB, or 36 pixels (3.24 km) on each side (Figure 22)
- 3) one pixel, or 90 m on each side (Table 7)

Table 6 lists the end-members and their areal abundances for a 8.1 km x 8.1 km region around the crater and a 3.24 km x 3.24 km region around the crater. The areal abundances of the image end-members, which were chosen by spectral distinctness, compare well to the areal abundances of the sample end-members, which are spectra of rock samples. One exception would be the areal abundance of the sample end-member Moenkopi Formation, which has a value of 0.000 for every pixel in the sample end-member analysis. Clearly, image end-member #3 (IEM#3) is evident in the image end-member analysis and most likely consists of local Moenkopi Formation plus some contaminants of the other two lithologies. During field work, it was evident that the Moenkopi Formation was not abundant on the scale of an ASTER TIR pixel size – 90 m

on each side or 8100 m² (0.0081 km²). Additionally, over the spectral resolution of ASTER, the spectral signature of the Moenkopi Formation is similar to a combination of approximately 75% Kaibab Formation and approximately 25% Coconino Sandstone.

The data for the other two lithologies clearly show that lithological mixing occurs in the image end-members. This clearly affects the results of the image end-member deconvolution, but is well within the 10% -15% accuracy predicted by *Ramsey* [2002a] where TIR data is deconvolved with 90-100 m pixels as lithologic end-members. As the areal abundance of the Moenkopi Formation in any ASTER pixel is below 15%, deconvolution with image end-members or sample end-members do not accurately represent the areal abundance of such lithologies.

4.3.2. Investigation of remotely-sensed properties

The investigation of the regions listed in section 3.6 are discussed here. The results of the TIMS image end-member analysis, ASTER TIR image end-member deconvolution, and the ASTER TIR sample end-member deconvolution are cropped to the same areal coverage of the crater and near-rim ejecta. The areal abundances for each end-member over the scenes are listed on Table 7.

1) The extent of northeast-trending windstreak:

The extent of the northeast-trending windstreak was measured on the TIMS and ASTER end-member analyses and subsequently compared. The windstreak is determined to cease where the areal abundance of the Coconino Sandstone (being either the sample end-member or IEM#1) is lower than 15%. This limit was chosen based on the results of previous studies that investigated the accuracy of deconvolving TIR spectra

[*Ramsey and Christensen, 1998; Feely and Christensen, 1999*] and estimated its accuracy with multispectral TIR data to be 10% – 15%. A previous TIR study of Meteor Crater predicted the confidence level of THEMIS image end-member analyses to be 10% to 15% [*Ramsey, 2002a*].

The extent of the windstreak in the TIMS end-member analysis was measured to be 2.4 km. For the ASTER image end-member analysis, the extent of the windstreak was measured as 2.7 km whereas the windstreak of the ASTER sample end-member analysis is 3.1 km. These measurements show the differences between the areal percentages of end-members and the errors associated with resolution degradation. As the spatial resolution is decreased, there is a loss of spectral distinctness between image end-members. As a result, the areal abundance of a certain image end-member will appear larger. In a previous study, the volume of Coconino Sandstone was estimated from the areal extent of the lithology as calculated from TIMS TIR data [*Ramsey, 2002a*]. Generally, this is not possible by remote sensing alone. If the calculation had been performed using the areal extent measured with ASTER rather than TIMS, the volume calculated would be increased. This is due to the areal extent of the windstreak measured with ASTER being higher than that on the end-member analysis using TIMS.

2.) The identification of one major and three minor zones in the windstreak:

It is clear from field work and high-resolution TIMS analysis that the Coconino Sandstone ejecta lies in four distinct zones. The southern CEB and northeast-trending windstreak has been discussed in detail and represents one zone. The other three zones are the Coconino ejecta lobes to the north of the crater (and west of the Visitor Center), northeast of the crater (and east of the Visitor Center), and east-northeast of the crater

(and described in Figure 27). Each of the four zones extends to the northeast due to southwesterly winds since crater formation and accounts for the northeast-trending windstreak.

All four zones are identified in both the TIMS and ASTER image end-member analyses, but their extent differs. This is due to the loss of spectral character as the spatial resolution is decreased. Because the spatial resolution is smaller, ASTER image end-members incorporate slight contaminations of other lithologies. This influences the results of an image end-member deconvolution.

3.) Eastern inner-crater strata and debris aprons:

Table 7 compares the areal abundance of the Coconino Sandstone end-member for each analysis. It should be noted that the spectral character of the Coconino end-member is different for each analysis (note the spectral plots of Figures 18, 19b, and 23). Further, the original emissivity data that is deconvolved varies for each analysis. However, Table 7 provides a quantitative comparison of the areal abundances for this end-member and demonstrates the effects of decreasing the spatial resolution of TIR data and their associated deconvolution.

The extent of Coconino Sandstone in the eastern inner-crater strata and debris aprons are not resolvable on the ASTER end-member analyses. This is an effect of resolution degradation and represents the loss of fine details in the TIR data as the spatial resolution is decreased from 3.2 m to 90 m.

4.) Areal abundance of the Coconino end-member:

Table 7 compares the areal abundances of the Coconino image end-member for the TIMS and ASTER end-member analyses. The Coconino image end-member

comprises 9.11 % of the TIMS scene and 14.19 % of the ASTER image end-member analysis. Clearly, the Coconino image end-member on the ASTER scene has incorporated a percentage of one or two of the other lithologies. This results in slight errors in the model results, and the areal abundances of 90-100 m image end-members will reflect this incorporation of other lithologies.

5.) Areal abundance of the Moenkopi end-member:

Table 7 shows the areal abundance of the Moenkopi end-member for the TIMS and ASTER end-member analysis. The Moenkopi Formation, with a low areal abundance and no large-scale (>8000 m²) outcrops, comprises 11.29 % of the TIMS image end-member analysis and 5.23 % of the ASTER image end-member analysis. These areal abundances also show the effects of resolution degradation associated with the selection of image end-members and the subsequent deconvolution with them. The distribution of lithologies with low areal abundances and no significant, large-scale outcrops will not be resolvable.

4.4. THEMIS TIR data

4.4.1. Temperature data

The daytime temperature is shown in Figure 30 with the scale of 0-255 DN values correlating to temperatures of 260 K to 274 K. The nighttime temperature is shown in Figure 30 with the DN values (0-255) ranging from 177 K to 190 K. The daytime and nighttime TIR scenes do not cover the exact same area. However, all of the CEB is contained on the daytime scene and the majority of the CEB is contained on the nighttime scene. This provides for a thermophysical comparison between the CEB and the

surrounding terrain. There is a significant correlation between the coldest temperatures in the daytime scene and the hottest temperatures of the nighttime scene both being contained in the CEB of the crater. This indicates that the pristine ejecta of the crater has a higher thermal inertia than the surrounding terrain and, thus, is composed of larger particle sizes than the surrounding plain. This agrees with earlier predictions that the rims and ejecta blankets of fresh impact craters will be composed of particle sizes that are larger than dust [Wright and Ramsey, 2002, 2003]. Because the low-albedo Syrtis Major region is composed of sand-sized particles [Palluconi and Kieffer, 1981; Christensen, 1983; Mustard et al., 1993; Bandfield, 2002], it is obvious that the ejecta blanket of this particular crater is composed of particles that are larger than sand.

As evidenced at Meteor Crater, the rims and ejecta blankets of fresh impact craters are composed of larger-than-dust particle sizes such as boulders, cobbles, pebbles, and sand [Shoemaker, 1960; Grant and Schultz, 1993] that are ejected and emplaced during impact [Wright and Ramsey, 2002, 2003]. These particle sizes are above the threshold size where TIR data are linearly additive [Moersch and Christensen, 1995; Ramsey and Christensen, 1998]. Therefore, the composition of the pristine ejecta can be determined via TIR spectroscopy.

4.4.2. Emissivity data and image end-member analysis

The daytime emissivity is used for the image end-member analysis as described in section 3.8 and a grayscale image of Band 3 (7.93 μm) is shown as Figure 13. Figure 31 shows a grayscale emissivity scene of Band 6. Similar to the other six bands, the impact crater and its ejecta blanket is not apparent on the image. This indicates the emissivities

of the pixels representing the crater rim, ejecta blanket, and the surrounding area are nearly identical. This is in contrast to the temperatures and relative thermal inertias of pixels, which clearly show differences in the rayed ejecta blanket, the crater rim, and local eolian transported material around the rim.

Spectral plots of two image end-members are shown as Figure 24 and are denoted as Image End-member A and Image End-member B. The image was deconvolved with the two image end-members and the results are shown as Figure 32a and 32b. Clearly, Image End-member A is the dominant member of the scene and accounts for 89.3% of the areal abundance as opposed to 7.0% for Image End-member B. An analysis of a 110 pixels by 110 pixels clip (~11 km by 11 km) of the crater, CEB, and local surrounding plain reveals that Image End-member A accounts for 94.4% of the areal abundance as opposed to 1.8% for Image End-member B. Figures 33a and 33b show the localized areas on the crater rim where Image End-member B has high (>90%) areal abundances. Due to the spectral similarity of the two end-members, this is most likely due to shallowing of spectral features due to particle size variations or slight topographic thermal variations. Another aspect is the approximate geometric correction performed for this analysis. Even slight geometric offsets may result in errors in the selection of image end-members and therefore the image end-member analysis. Due to the dominance of Image End-member A, it is possible that the spectrum of this image end-member represents the lithology of the entire scene, including the crater rim and ejecta.

Both THEMIS image end-members appear to be basaltic in nature. The location of absorption features agrees with those of Mars Surface Type 1 (ST1) [*Bandfield et al.*, 2000]. The particle size of the surface sediments is beyond the scope of this work.

Mustard et al. [1993] and *Bandfield* [2002] agree that this region of Syrtis Major is composed of sand-sized, basaltic sediments.

RMS errors for the THEMIS image end-member deconvolution range from 0.001 to 0.030 with the average RMS error of the scene being 0.017. Where the sum of the areal abundances of the two end-members do not sum to 100%, the RMS error is increased. RMS error images are displayed as Figures 34 and 35. As shown with the overall low mean RMS error (1.7%), the majority of the pixels exhibit RMS errors of less than 2.0%. Figure 35 displays all RMS errors greater than 2.0%. Portions of the crater's ejecta blanket and most of the crater floor have the highest RMS errors. This is shown in Figure 36. In these areas, shadows or incorrect geometric corrections likely result in the "poor fit" of the spectra to the two image end-members.

5. Conclusions

Analyses of ASTER TIR data of Meteor Crater provide excellent analogs to develop and test a methodology to examine a large quantity of similar TIR data from the THEMIS instrument. Meteor Crater is a unique terrestrial site in which the results of analyses performed with spaceborne data sets can be validated with field observations, and this provides insight into studying similar-sized martian impact craters with remote sensing alone. Topics of investigation may include crater deterioration, ejecta distribution, and/or ejecta composition.

Through fieldwork at Meteor Crater, Arizona, analysis of both airborne and spaceborne TIR data of Meteor Crater, and analysis of THEMIS TIR data of a small impact site on Mars, this work has resulted in several significant findings.

The rims and ejecta blankets of fresh impact craters have a higher thermal inertia than that consistent with particles that are greater than dust-sized. Due to this, the rims and ejecta blankets of fresh impact craters in the high-albedo, dusty regions are excellent targets for thermal infrared spectroscopy. The TIR spectra of the pixels representing a young crater's rim and ejecta blanket may provide insight into the composition of underlying lithologies or bedrock underlying the dust.

Deconvolving THEMIS TIR data with selected image end-members can be used to constrain quantitative measures of the surface distribution of ejecta for fresh impact craters on Mars. Specifically, in conjunction with other data sets and previous works on the structure and erosional states of impact craters, the areal abundance of an image end-member in an ejecta blanket, windstreak, or inner-crater strata can provide estimates of local stratigraphy and weathering rates.

The use of image end-members with multispectral thermal infrared data such as ASTER or THEMIS is useful, but the image end-members should be chosen with caution or with statistical analysis. Image pixels that are the most spectrally distinct should contain the least mixing of lithologies and serve as image end-members.

If chosen correctly, image end-members provided better model fits than laboratory emission spectra where spaceborne TIR data are deconvolved. Image end-member percentages between the spaceborne ASTER data and hi-resolution airborne TIRS data varied by < 10% on average. It is obvious that local lithologic mixing occurs as a result of the instrument's 100 meter spatial resolution. There are at least two complicating factors. Separation of lithologies with similar spectral signatures over the TIR channels used for an image end-member deconvolution are difficult. Lithologies

need to have a distinct spectral signature over the multispectral TIR bands for a precise selection of image end-members and a subsequent accurate deconvolution to occur.

Detection of lithologies with low areal abundances are also difficult. If a lithology does not have a large areal abundance over any one pixel, a statistical analysis over the scene's pixels may not yield an image end-member than contains the lithology. Conversely, the selection of a pixel than contains the lithology plus other, separate lithologies to be an image end-member will affect the results of the image end-member deconvolution. The distribution of ejecta will actually yield the distribution of the limited lithology where it exists with the other lithology or lithologies found in the image end-member. This should be noted by the scientist performing the image end-member analysis.

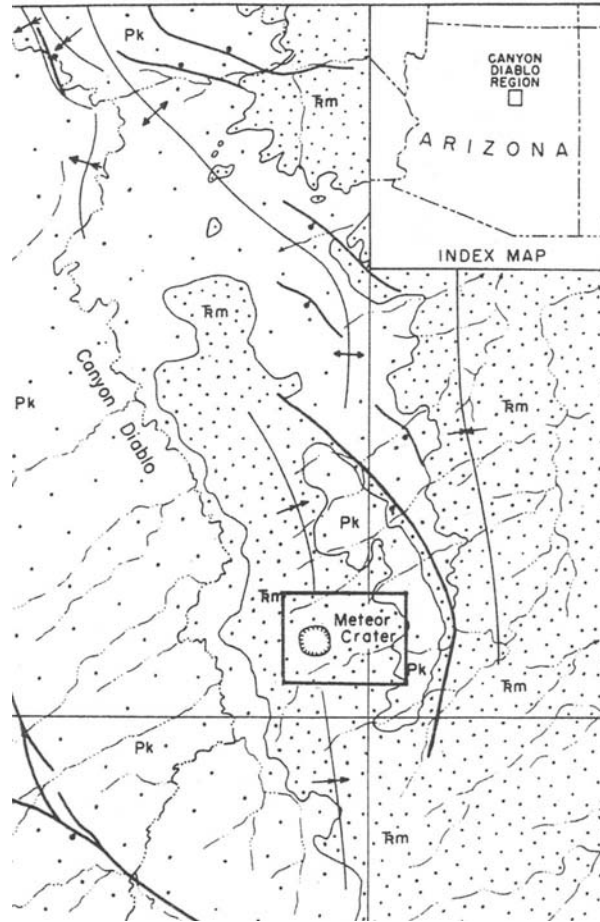


Figure 1 **Location of Meteor Crater**

The figure (modified from [Shoemaker and Kieffer, 1974]) displays the regional geology of the Canyon Diablo region consisting of surface exposures of the Permian Kaibab (Pk) Formation and the Triassic Moenkopi (Trm) Formation. The latitude line on the map is 35° N and the longitude line is 111° W. For scale, Meteor Crater is 1.2 km in diameter. The crater's precise location is 35° 01'N, 111° 01'W.

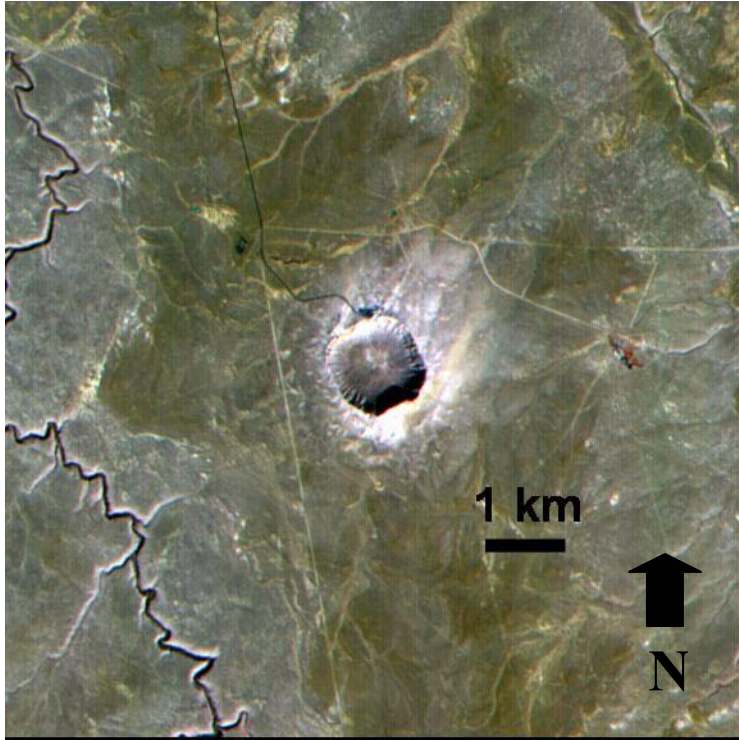


Figure 2 ASTER VNIR image of Meteor Crater

ASTER bands 3, 2, and 1 are represented by the colors red, green, and blue, respectively. As chlorophyll-containing vegetation reflects NIR energy and this is detected by ASTER band 3, vegetation shows up as red. It is evident from the image that the only abundant green vegetation is located on a farm ~2.5 km east of the crater.




<u>Lithologic Picture</u>	<u>Formation Name</u>	<u>Age</u>	<u>Symbol</u>
	Moenkopi Formation	Triassic	Tm
	Kaibab Formation	Permian	Pk
	Coconino Sandstone	Permian	Pcs

Figure 3 Stratigraphic Column

Only the three primary lithologies are shown. See text for lithologic descriptions and stratigraphic thicknesses.

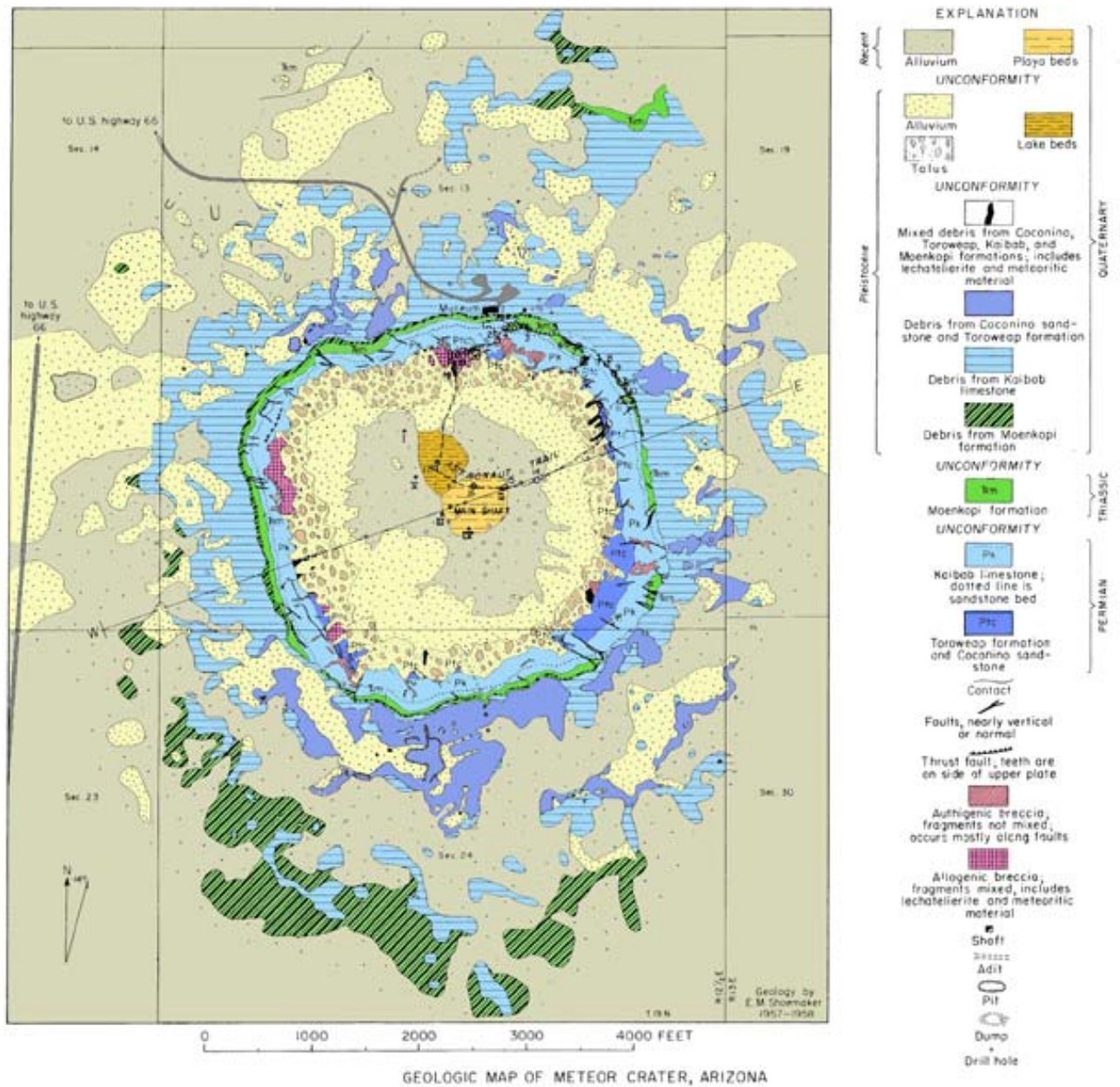


Figure 4 Geologic map modified from *Shoemaker* [1960, 1963; *Shoemaker and Kieffer*, 1974].

Shoemaker mapped surface exposures of the original and ejected components of each lithology.

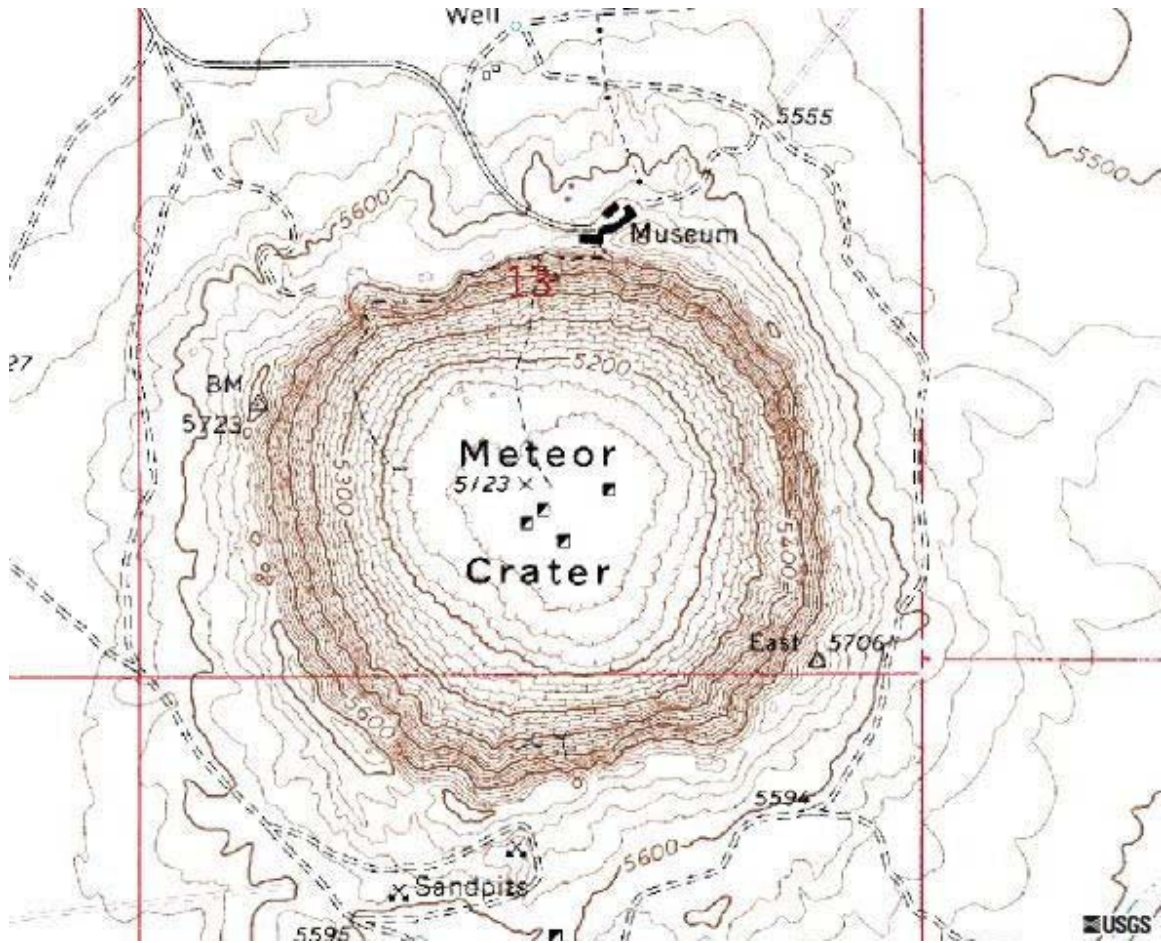


Figure 5 USGS Contour map of Meteor Crater

The contour map has a contour interval of 20 m. Paved roads are denoted with double straight lines and unpaved roads with double dashed lines. The half-filled squares and crossed shovels represent the locations of drill holes and mines, respectively.

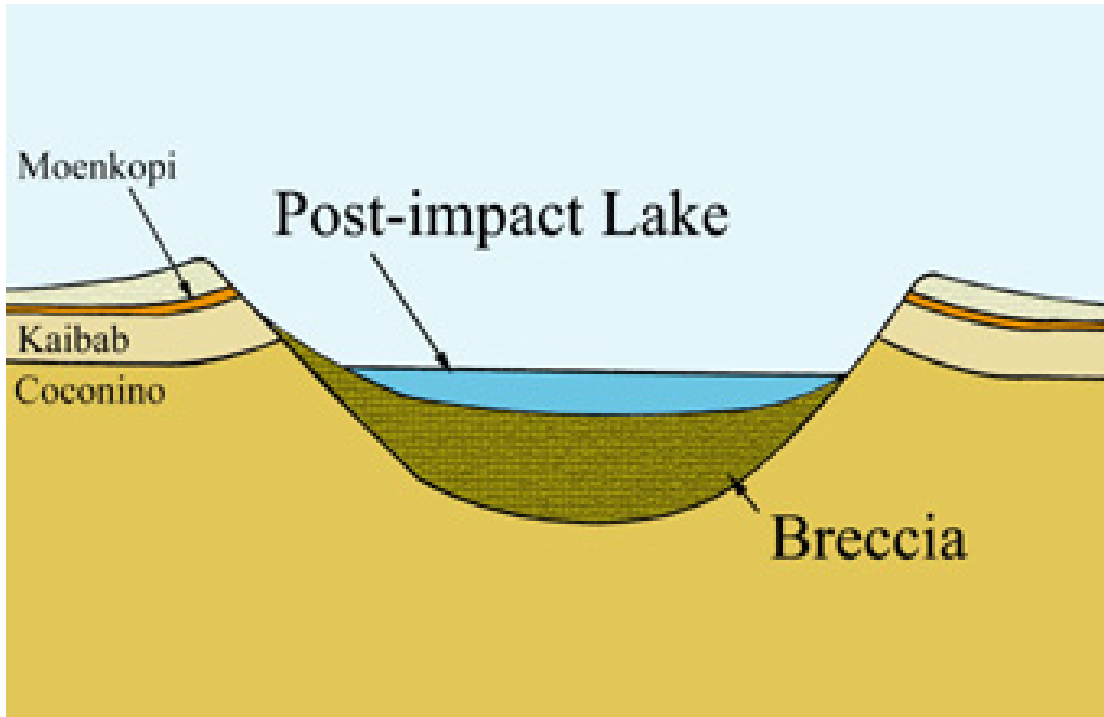


Figure 6 Schematic diagram of Meteor Crater

The schematic diagram depicts the uplifted strata, impact breccia, and post-impact lake.

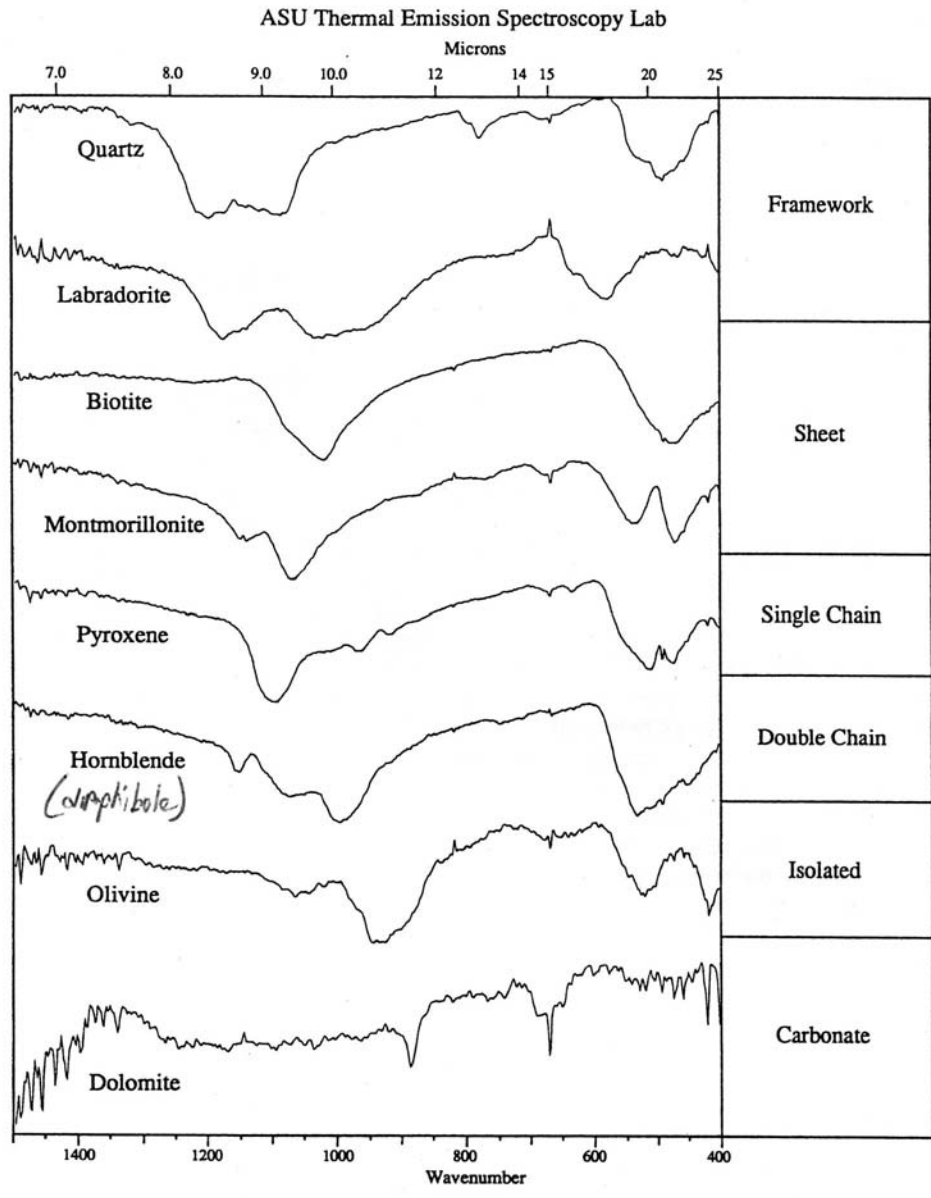


Figure 7 Thermal infrared spectra of common rock-forming minerals (modified from *Christensen et al.* [1992])

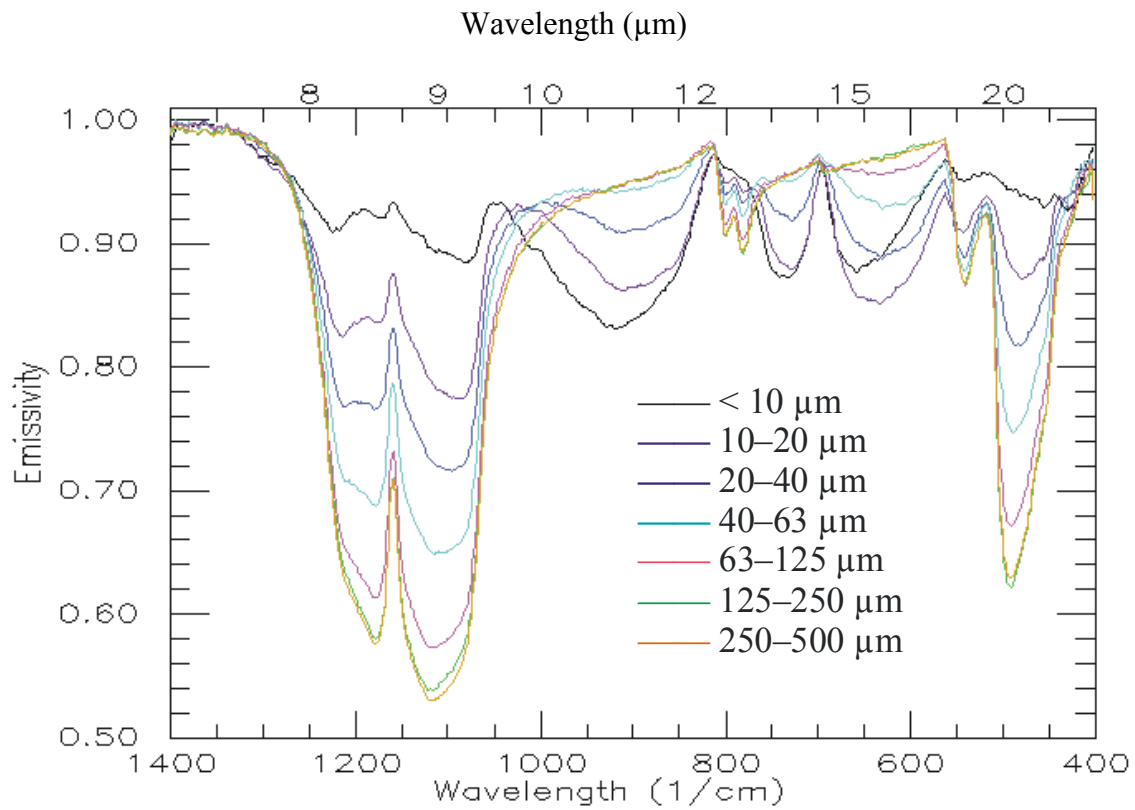


Figure 8 TIR laboratory spectra of various particle sizes of quartz (adapted from [Ramsey and Christensen, 1998])

It is obvious that the depth of absorption features (restrahlen bands) decreases as the particle size of quartz decreases, but the position of the restrahlen band does not. In spectral regions that are not restrahlen bands, the depth increases as the particle size is decreased.

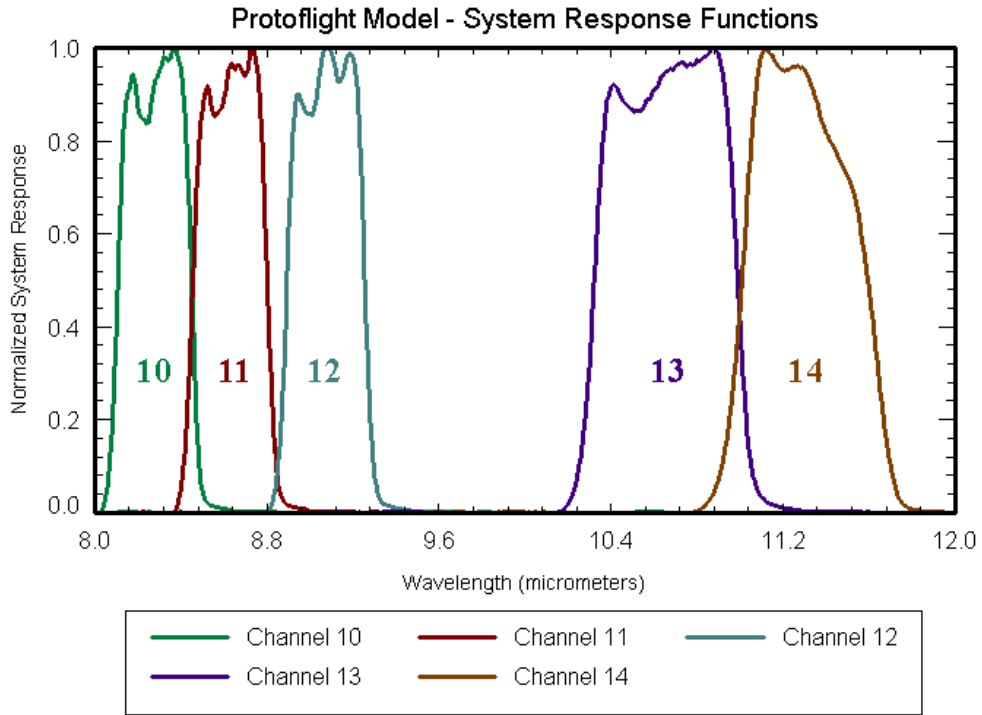


Figure 9 TIR spectral response functions for the Advanced Spaceborne Thermal Emission and Reflection Radiometer (ASTER) instrument.

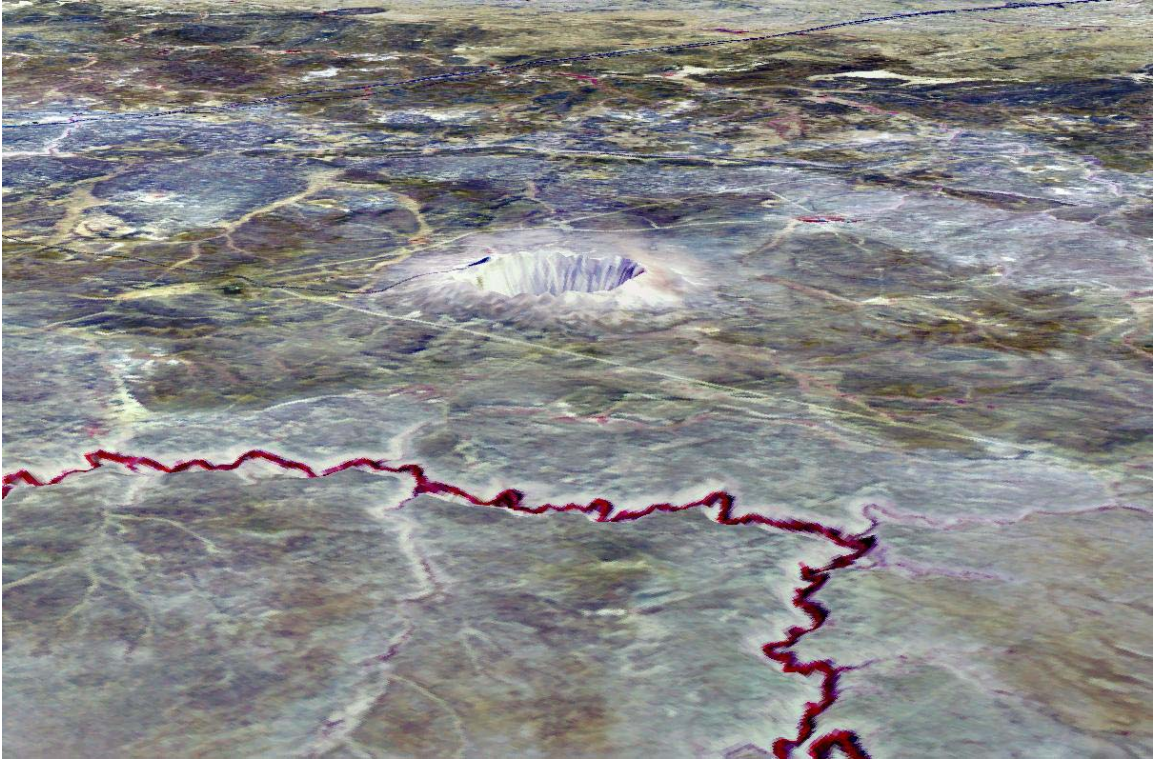


Figure 10 Digital Elevation Model (DEM) of Meteor Crater

The DEM, with view to the NE, was produced using a nadir-pointing (Band 3N) and a backwards-pointing (Band 3B) VNIR band on the ASTER instrument.

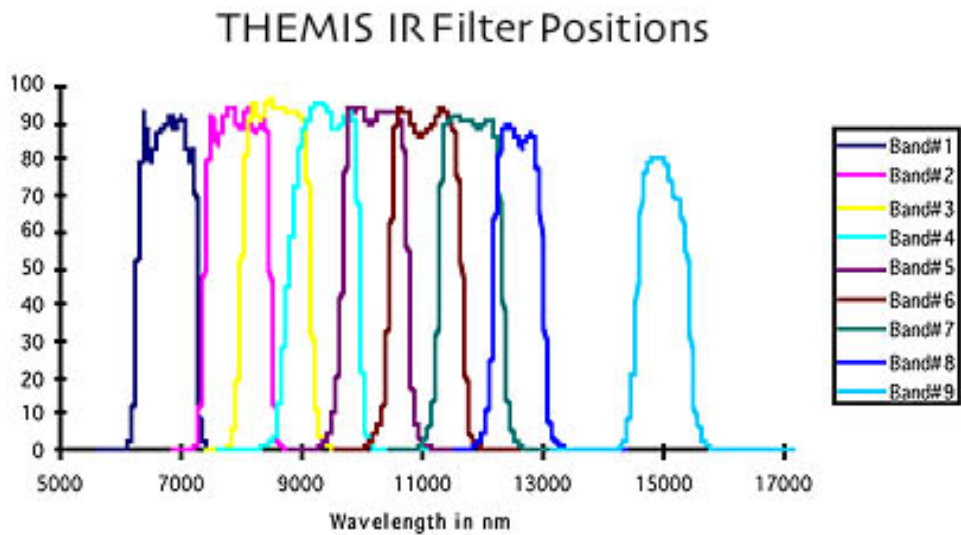


Figure 11 TIR Spectral response functions for the Thermal Emission Imaging System (THEMIS) instrument on the 2001 Mars Odyssey spacecraft.

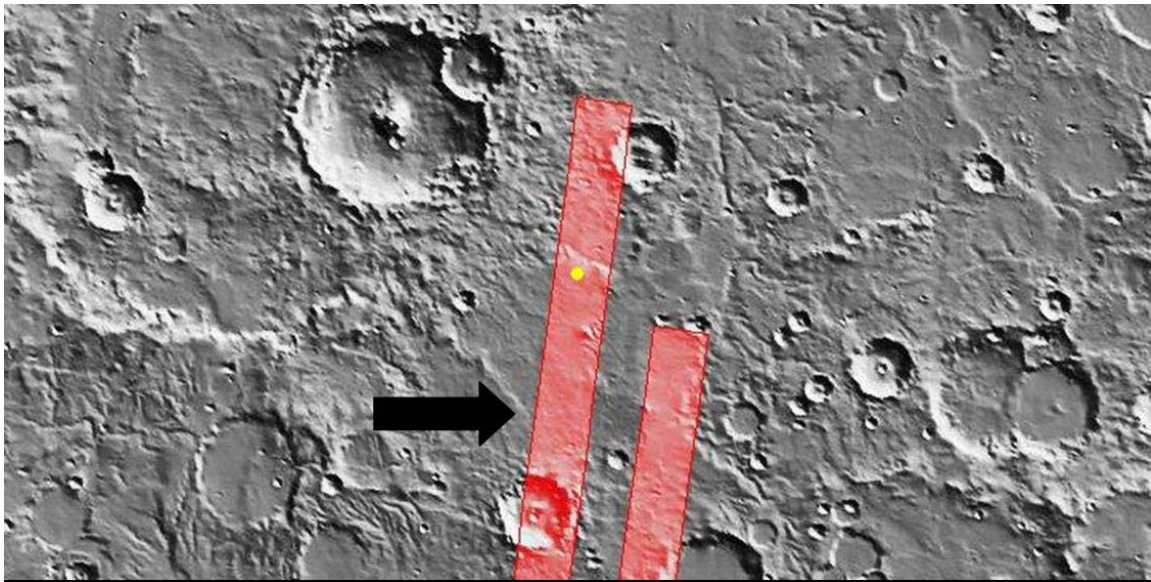


Figure 12 Location of impact crater under investigation with daytime TIR strip

The black arrow points to THEMIS daytime TIR strip I01297001 and the yellow circle shows the approximate position of the crater. The IR strip is 32 km across and the crater is located at 4° S, 59° E in southwest Syrtis Major.



Figure 13 Daytime THEMIS scene I01297001

The TIR radiance of Band 3 ($7.93 \mu\text{m}$) is shown. The scene is 32 km across and the crater is located at approximately 4° S , 59° E in southwest Syrtis Major. The rim to rim diameter of the crater is approximately 1.1 km. The crater ejecta appears to have a lower radiance than the surrounding plain during the day.

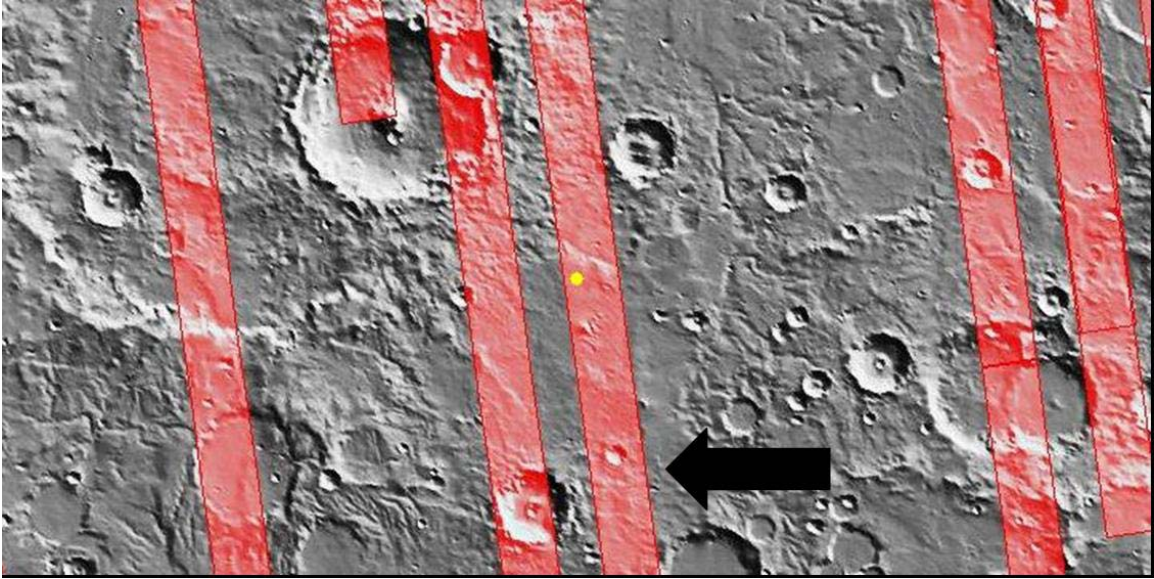


Figure 14 Location of impact crater under investigation with nighttime TIR strip

The black arrow points to the nighttime THEMIS TIR strip used in this study. For scale, the strip is 32 km across. The yellow circle indicates the approximate position of the crater at 4° S, 59° E in southwest Syrtis Major.

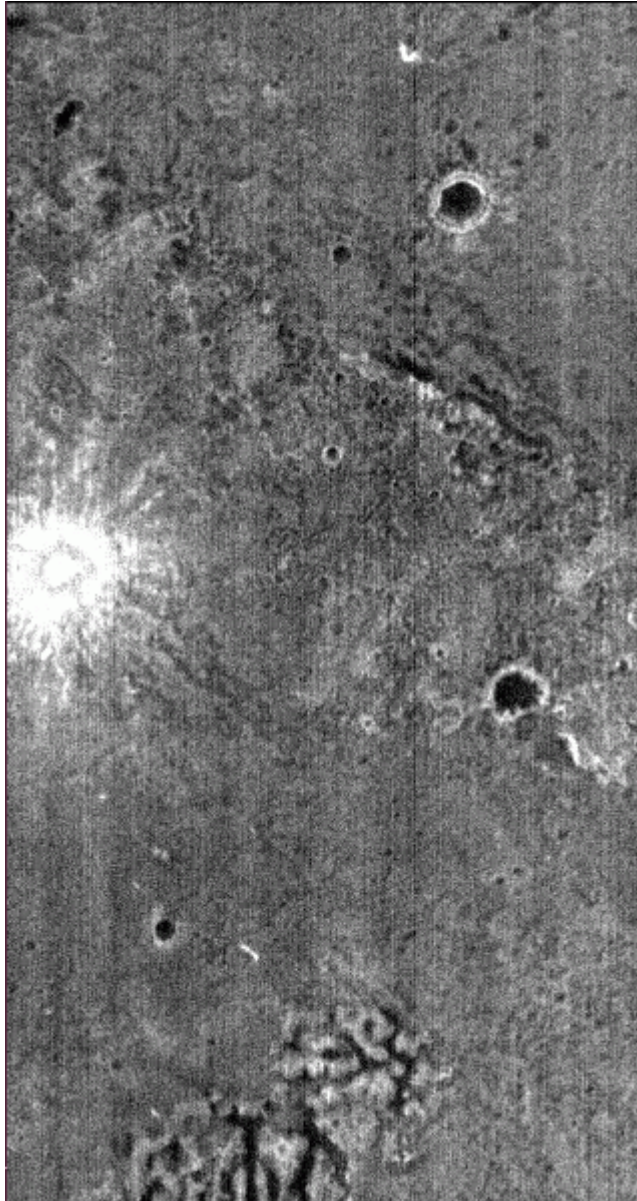


Figure 15 Nighttime THEMIS scene I01852006

The TIR radiance of Band 9 (12.57 μm) is shown. For reference, the scene is 32 km across. The crater ejecta appears to have a higher radiance at night than the surrounding terrain.

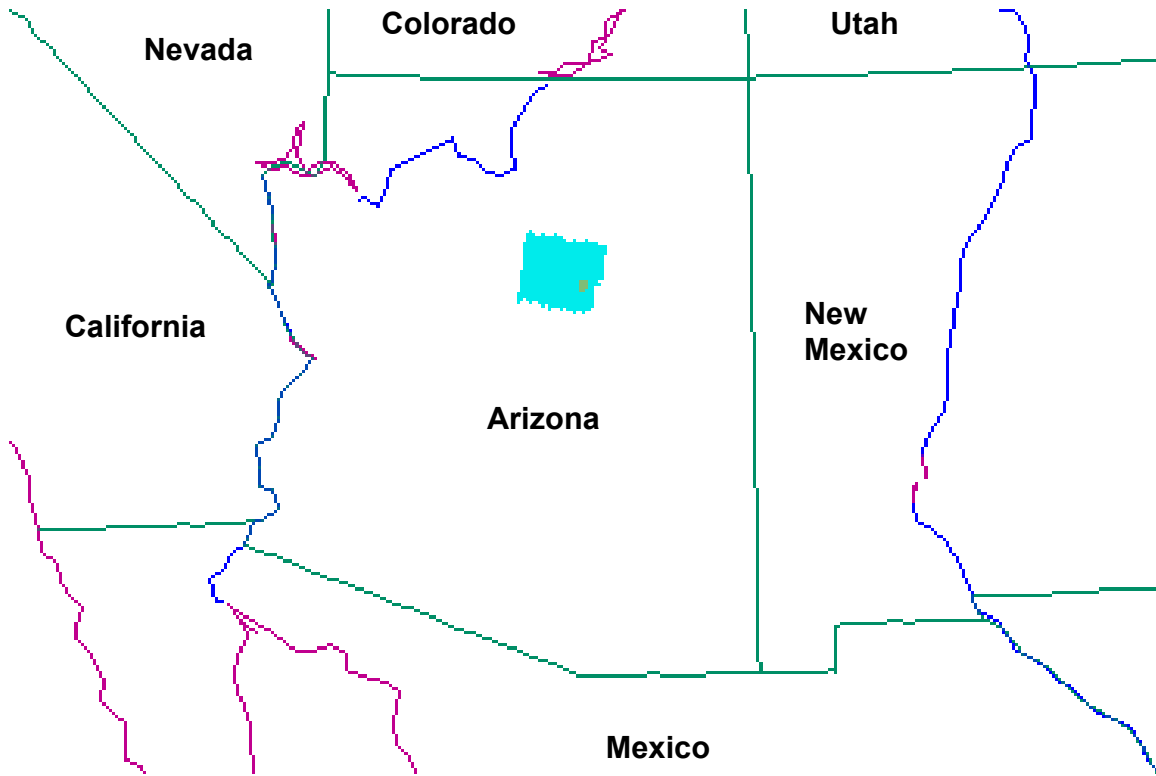
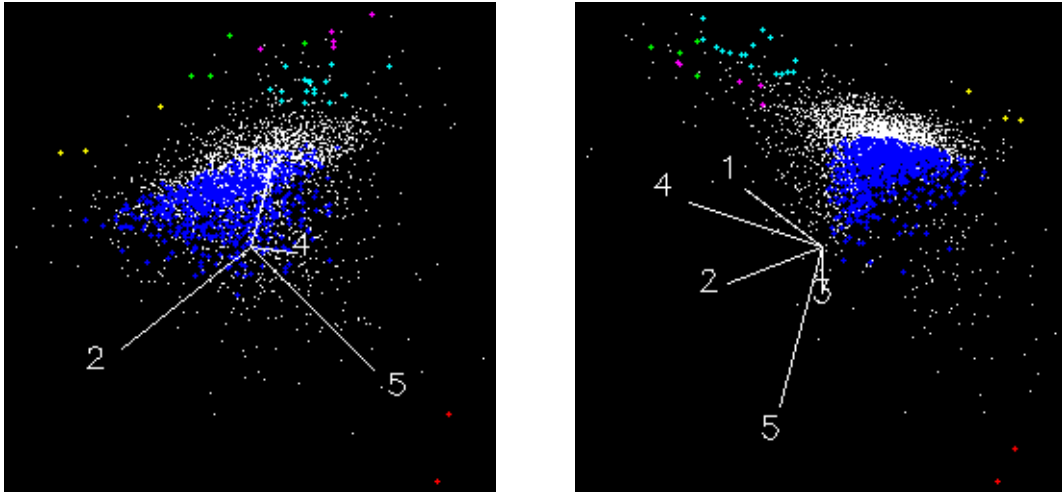


Figure 16 ASTER Coverage

The small rectangle highlighted in cyan represents the coverage of the ASTER data scene used in this study. The rectangle is 72 km across and 60 km wide. Table 5 lists the Granule ID's of all data levels for the scene.



Figures 17a and 17b Cluster of 5-dimensional data

The above figures illustrate the 5-dimensional cluster of data that is used to plot the 5 bands of ASTER TIR emissivity data. The most spectrally distinct pixels are chosen to be image end-members.

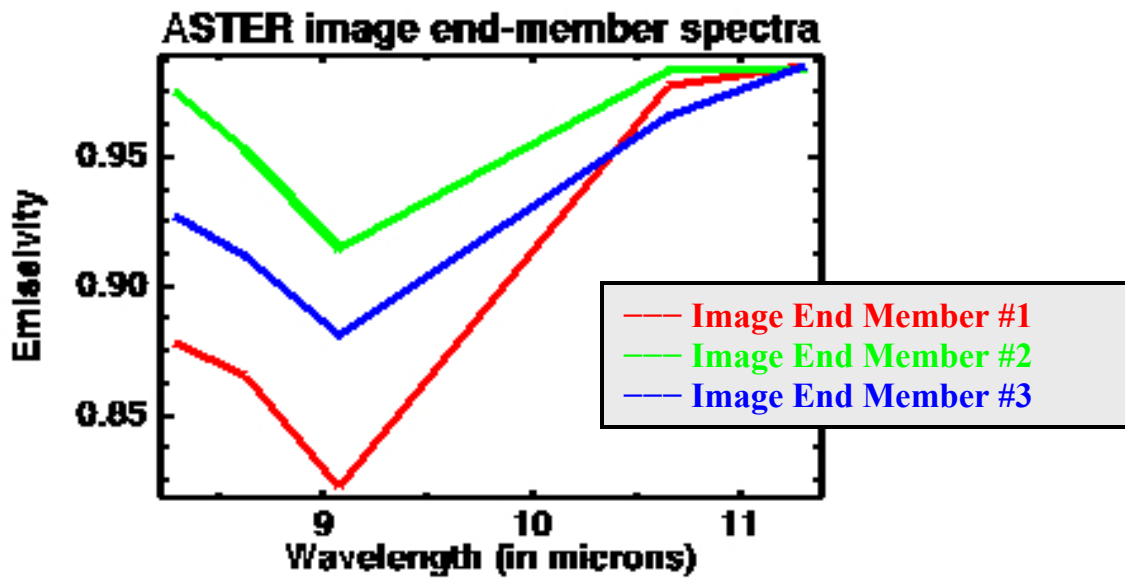


Figure 18 ASTER TIR Image End-Member Spectra

Three image end-members are selected from the Spectral Mapping Wizard algorithm in ENVI.

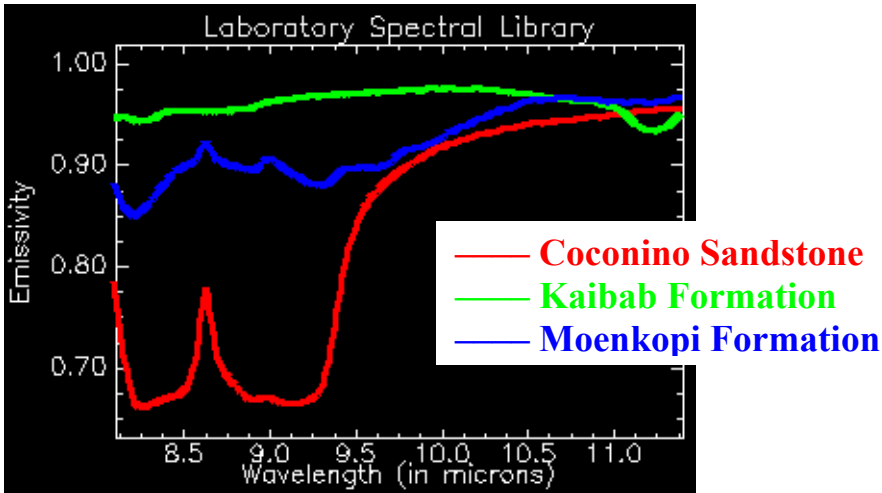


Figure 19a Laboratory Spectra of Meteor Crater lithologies

Emissivity plots for hand samples of three lithologies are displayed. Thermal emission spectra represent the tops of weathered samples.

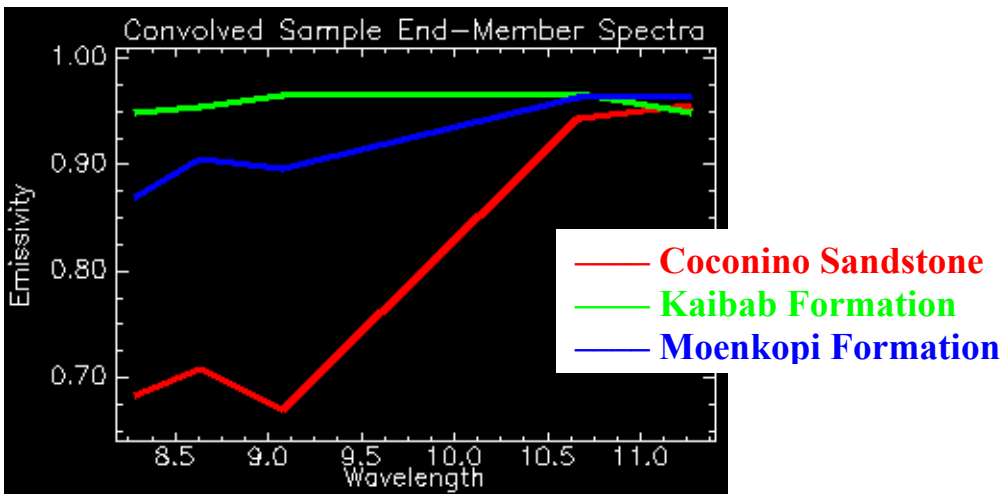
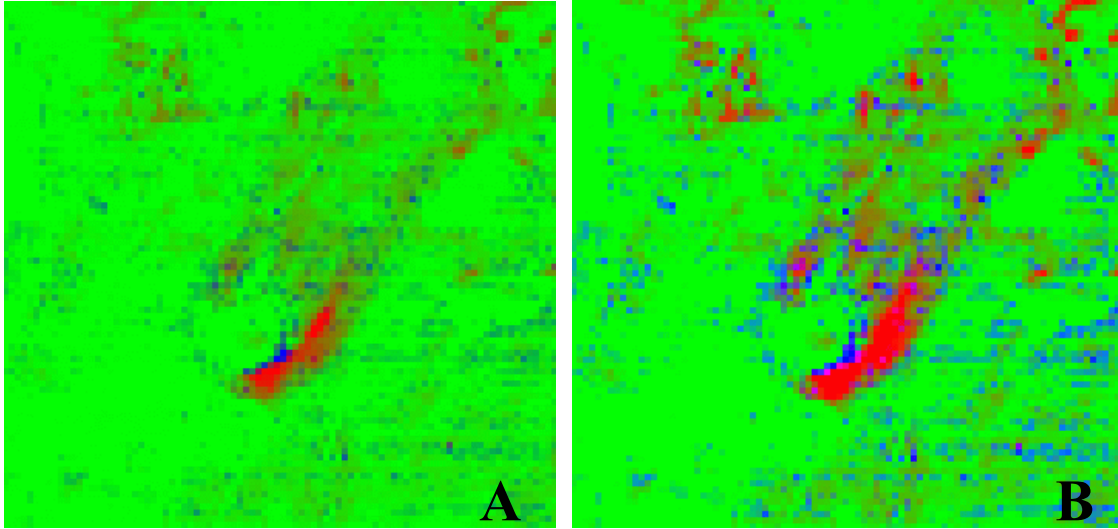


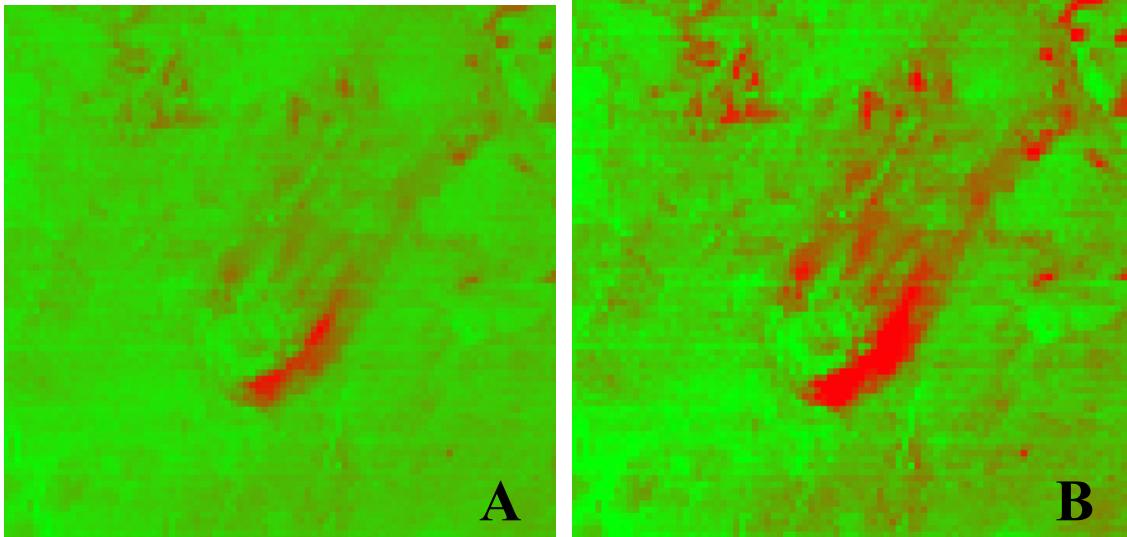
Figure 19b Convolved Sample End-Member Spectra

The 198-point data displayed in Figure 19a is convolved using ASTER TIR spectral response functions. The color scheme is the same as that for Figure 19a.



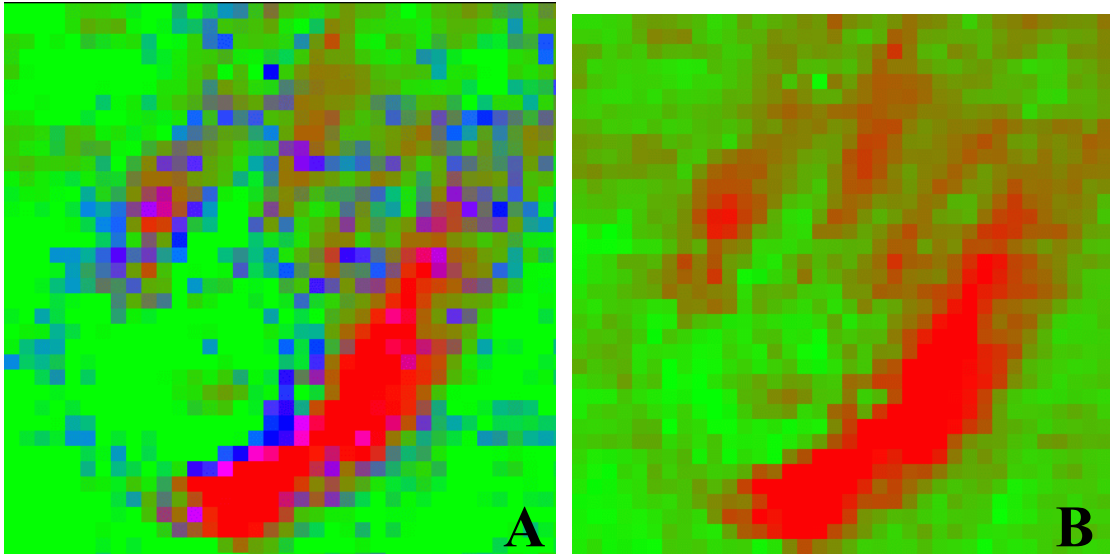
Figures 20a and 20b Image End-Member Analysis (0% stretch)

The above figures represent the deconvolution of an ASTER emissivity scene of Meteor Crater with three image end-members. The color scheme is identical to that of Figure 18, which displays spectral plots of the image end-members. The colors in Figure 20a (on the left, designated by “A”) represent the areal abundance of each image end-member. For Figure 20b, the areal abundances have been stretched 1% to better show the distribution of the three image end-members (see text for more details). Each scene is 90 pixels by 90 pixels, or 8.1 km on each side. North is up.



Figures 21a and 21b Sample End-Member Analysis

The deconvolution of an ASTER emissivity scene with three sample end-members is shown. The color scheme is identical to that of Figures 19a and 19b, which displays the spectral plots of the sample end-members. Figure 21a represents the true areal abundances. The data comprising the sample end-member analysis is stretched 1% in Figure 21b to visually show the calculated areal percentages of each sample end-member. The Moenkopi sample end-member has an areal abundance of 0.000 for all pixels in the sample end-member analysis.



Figures 22a and 22b **Comparison of ASTER end-member analyses**

Figures 22a and 22b are close-ups of the approximate extent of the continuous ejecta blanket (CEB). Figure 22a is an image end-member analysis (see text and Figures 18 and 20 for end-member plots and analyses, respectively, for more details). Figure 22b is the same region of the CEB, but is a sample end-member analysis (see text and Figures 19 and 21 for end-member plots and analysis, respectively).

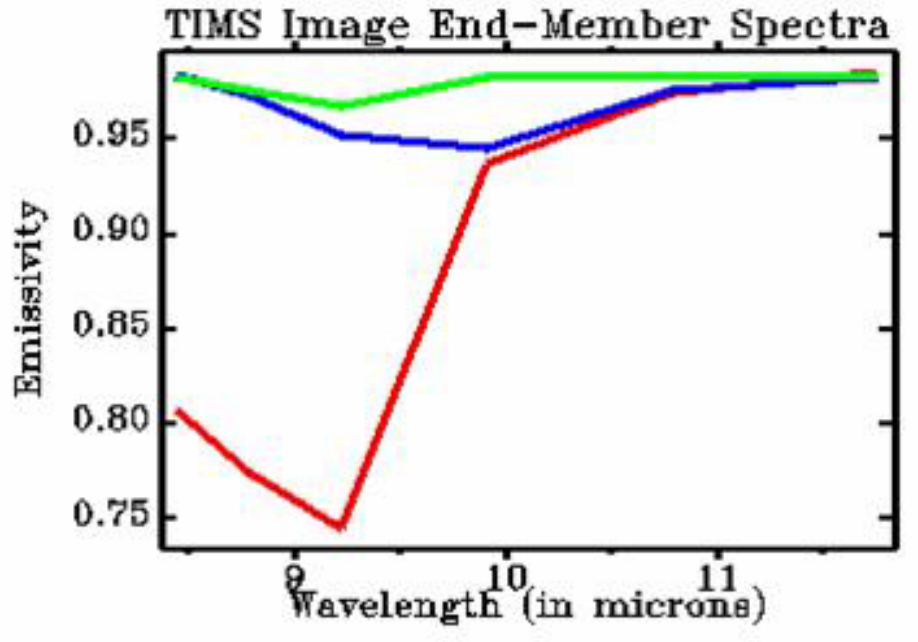


Figure 23 Spectral plots of TIMS image end-members

The emissivity data from the six bands of the TIMS instrument were plotted against each other in six dimensions. The image end-members were chosen by an algorithm in an image software program designed to choose the most spectrally-distinct pixels. The image end-member spectra corresponds to Coconino Sandstone (in red), Kaibab Formation (in green), the Moenkopi Formation (in blue) and to the spectra provided by an earlier study of Meteor Crater using TIMS data [Ramsey, 2002a].

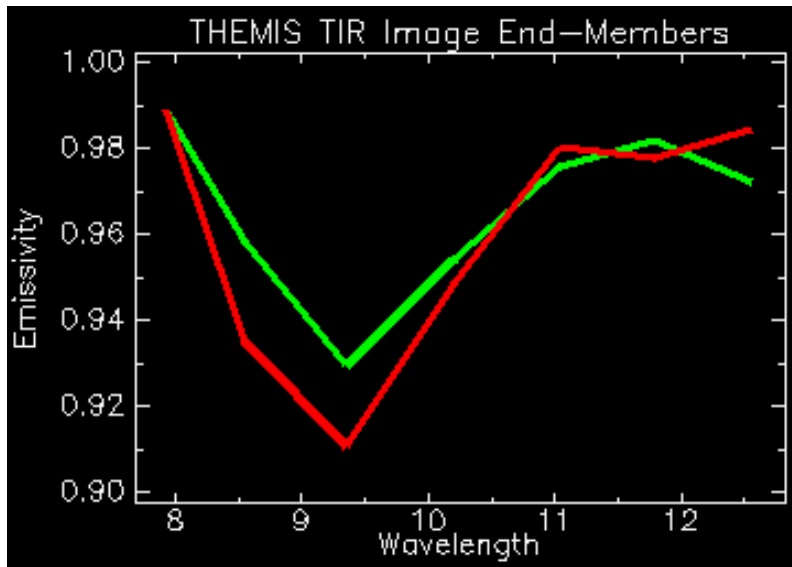


Figure 24 THEMIS TIR image end-member spectra

An image processing software algorithm is used to select the most spectrally distinct pixels to be image end-members for the THEMIS emissivity scene. This is identical to the methodology used to select image end-members for the ASTER and TIMS image end-member analyses.



Figure 25 **RMS error image of ASTER TIR image end-member analysis**

The area in the RMS error image is identical to that covered by the ASTER image end-member analysis shown in Figure 20. The scene is composed of 90 pixels by 90 pixels, or 8.1 km on each side. Data has been stretched so that a DN value of 0 is equal to 0.0% and a DN value of 255 is equal to 0.5%, or 0.005. North is to the top of the image.



Figure 26 **RMS error image of ASTER TIR sample end-member analysis**

The data has been stretched so that a RMS error of 2.0% or less has been set to a DN of 0 whereas a RMS error of 2.5% or more has been set to a DN of 255. The image covers an area that is 90 by 90 ASTER pixels, or 8.1 km on each side. The circle of the low RMS errors (shown as the darkest pixels) represent the crater rim and have RMS errors of less than 0.020.

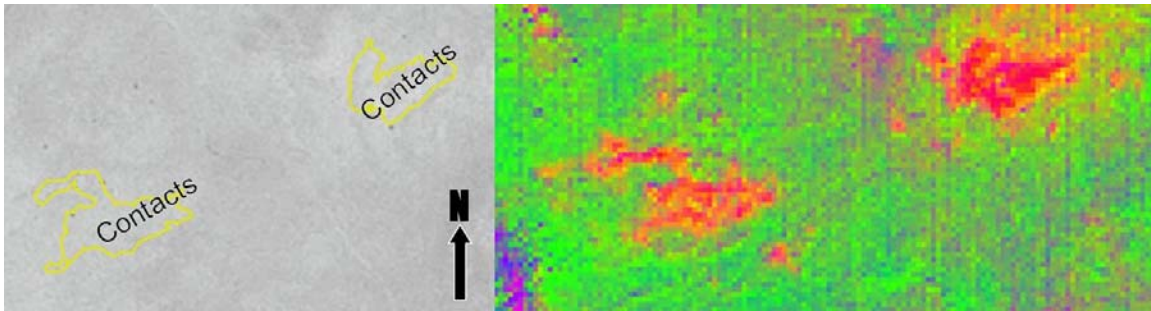


Figure 27 Field work validates TIMS image end-member deconvolution

On the eastern, near-field CEB, the boundaries of ejecta lobes of Coconino Sandstone on top of Kaibab Formation were recorded with a GPS unit (shown on left image as a yellow line on top of a Digital Orthogonal Quarter Quadrangle (DOQQ)). From the TIMS image end-member analysis on the right, it is clear that the lobes (shown as red Coconino with green Kaibab) are nearly identical to that recorded in the field.

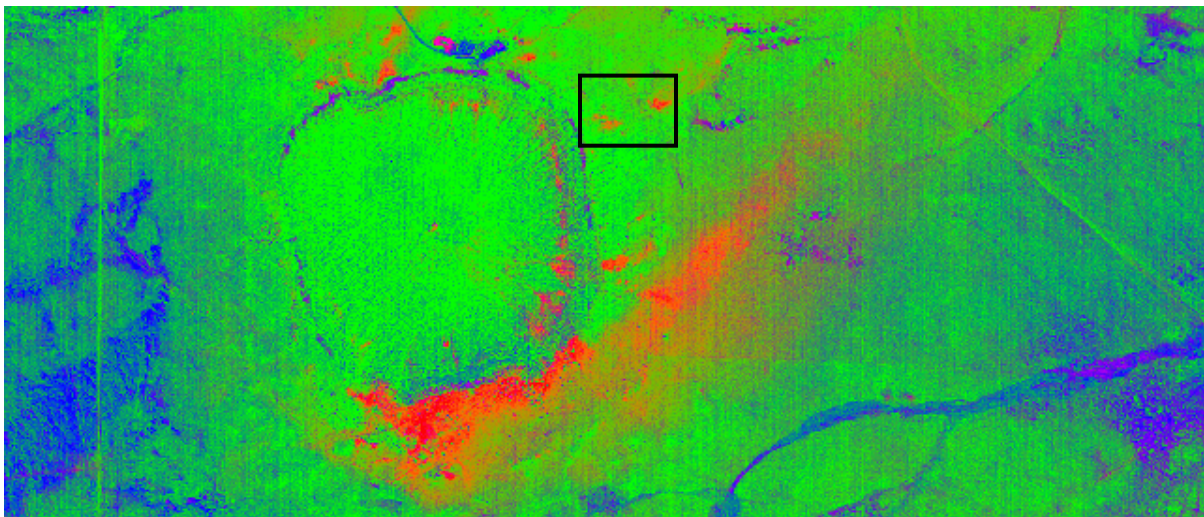


Figure 28 TIMS image end-member analysis

The TIMS emissivity scene is deconvolved with three image end-members shown in Figure 23 to produce the above analysis. The color scheme is the same as that for Figure 23, with each color representing the areal distribution of the end-member. Image is stretched 1% for visualization purposes. The rectangular box northeast of the crater rim is the approximate area covered in Figure 27.

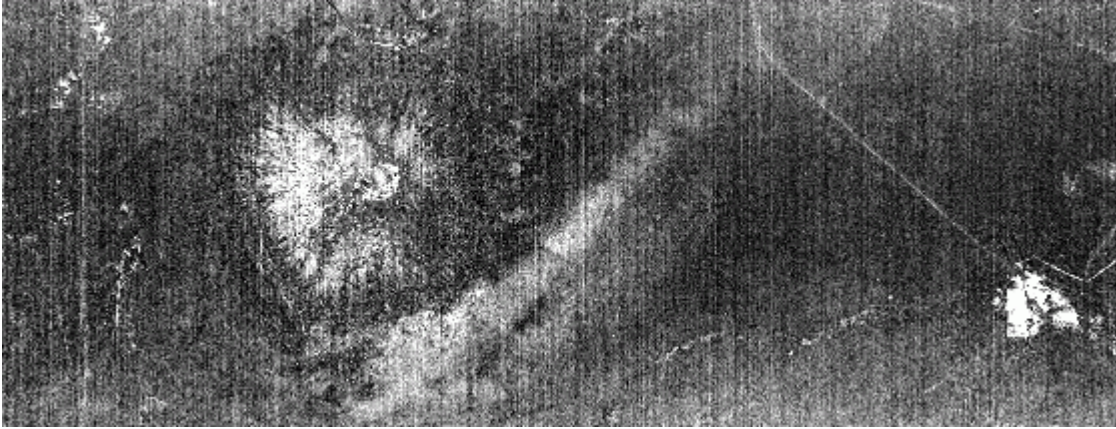


Figure 29 RMS error image of TIMS image end-member analysis

The RMS error from the deconvolution performed to create Figure 28 is displayed here. A DN of 255 (white) represents 0.010 and high RMS errors or “poor fits”. A DN of 0 (black) represents a RMS error of 0.000, little to no RMS error, and “good fits”.

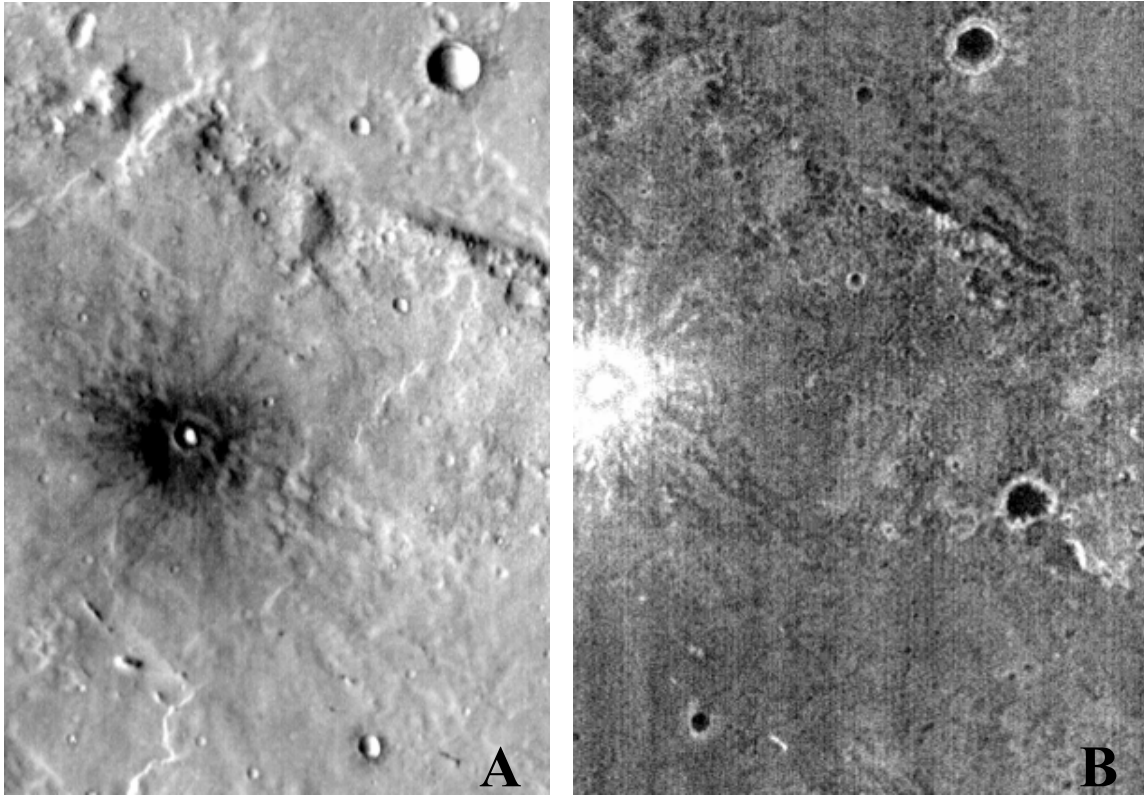


Figure 30a and 30b **Temperature scenes of an impact crater in Syrtis Major**

The figures show the difference in thermal inertia between the crater ejecta and the surrounding plain. The two scenes do not cover the exact same area, but the crater is evident in both. The pixels representing the crater ejecta are 14 K cooler than the surrounding regions during the daytime scene (Figure 30a) and 13 K hotter on the nighttime scene (Figure 30b).

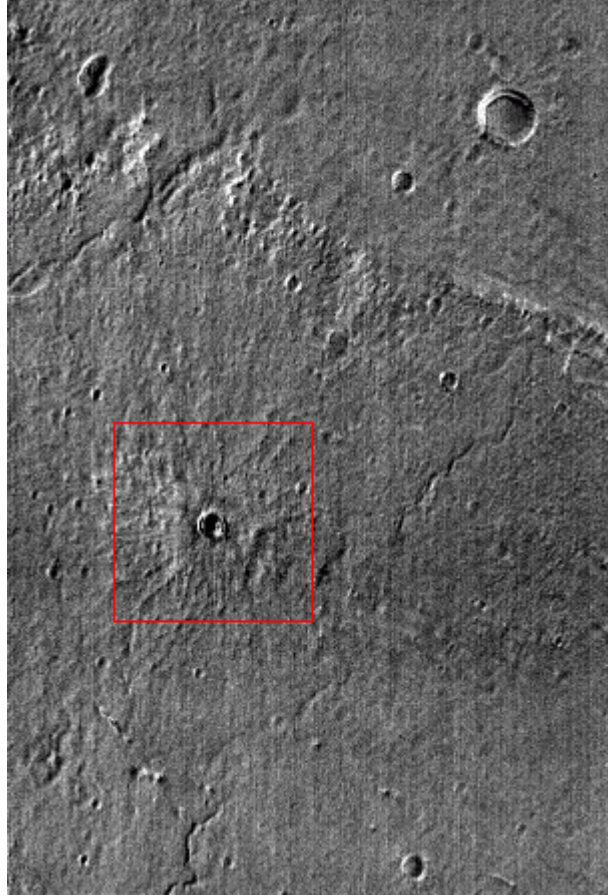


Figure 31 Emissivity scene of the crater in Syrtis Major

The scene covers the same area as the daytime radiance and temperature scenes (Figures 13 and 30a, respectively). The emissivity of Band 6 is shown. The data is stretched so that DN values of 0 to 255 represent emissivities of 0.880 to 0.950. The approximate area covered by the crater and CEB is boxed in red.

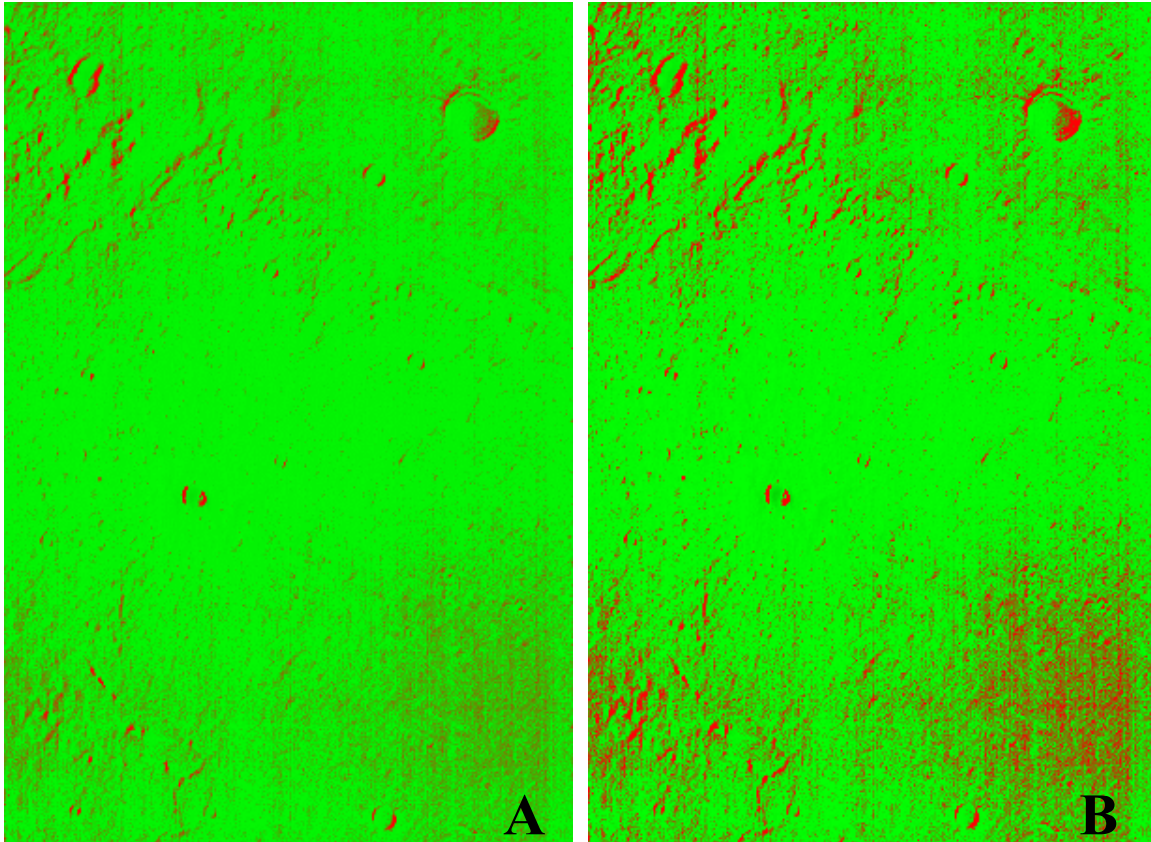


Figure 32a and 32b **THEMIS image end-member analysis**

The emissivity data of the THEMIS daytime scene I01297001 was deconvolved using the image end-members displayed in Figure 24. The color scheme is the same as that for Figure 24, with green representing areal distribution of the green image end-member and red representing the distribution of the red image end-member. For Figure 32a, the areal abundance data is not stretched. DN values of 0-255 represent areal abundances of 0% - 100%. The data is stretched 1% for Figure 32b to better display the areal abundance of the red image end-member. See text (section 4.4) for comments on the lithologies and their areal abundances. North is at 10:00.

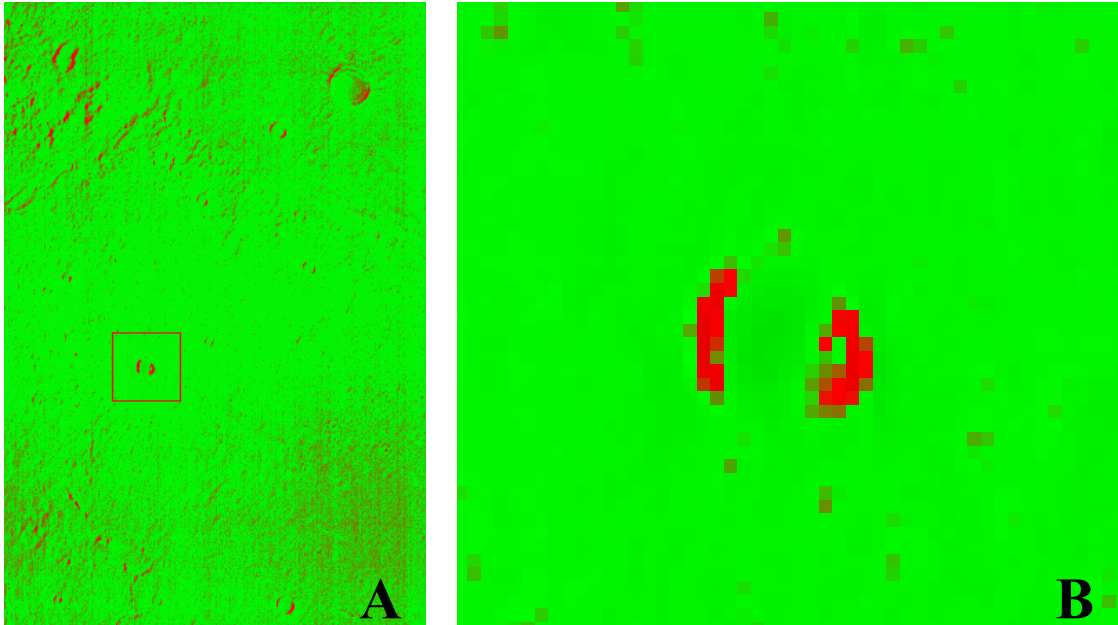


Figure 33a and 33b **Extent and close-up of CEB of Figure 32a**

The red box in Figure 33a shows the extent of Figure 33b. Figure 33a represents the THEMIS image end-member analysis from Figure 32a. Figure 33b shows the areal distribution of the red image end-member (from Figure 24) on the northwestern and southeastern rim of the crater. North is at 10:00. Due to the spectral similarity of the two THEMIS image end-members, this may be due to particle size variations and associated absorption band depth between this portion of the rim and the rest of the scene.



Figure 34 RMS error image of THEMIS image end-member deconvolution

DN values of 0-255 represent RMS errors of 0.0% to 3.0%. The scene is 32 km across.

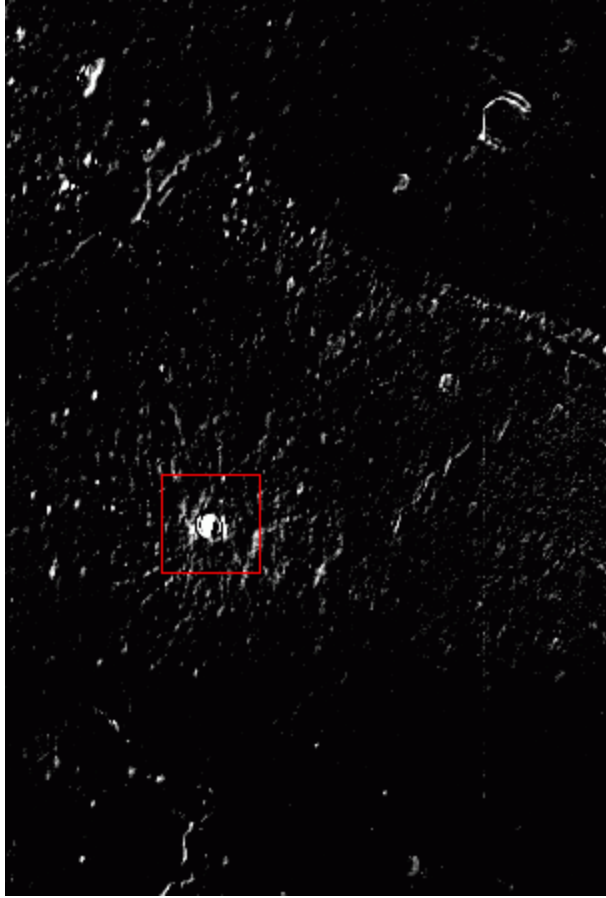


Figure 35 RMS error image of THEMIS image end-member deconvolution

The RMS error image shown as Figure 34 is stretched to enhance the highest RMS errors. DN values of 0-255 represent RMS errors of 2.0% to 3.0%. The red box outlines the near-rim CEB and the coverage for Figure 36. Clearly, the crater interior and rim have the highest RMS errors along with other topographic boundaries in the scene such as ridges and eroded crater rims.

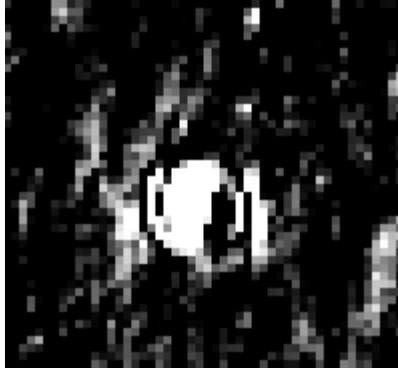


Figure 36 Close-up of RMS errors associated with CEB

The red box in Figure 35 shows the extent of Figure 36. The data range is identical to that of Figure 35, with DN values of 0-255 representing RMS errors of 2.0% to 3.0%.

Table 1. Thermal Infrared Instruments on Mars-orbiting Spacecraft

Instrument	Spacecraft	Spectral Resolution	Spatial Res. (km)
IRS	Mariner 6 & 7	hyperspectral from 2 – 14 μm	~150
IRR	Mariner 6 & 7	2 bands at 10 μm & 20 μm	~50
IRR	Mariner 9	2 bands at 10 μm & 20 μm	15 - 100
IRIS	Mariner 9	hyperspectral from 5 – 50 μm	>110
IRTM	Viking I and II	5 bands: 7, 9, 11, 15, 20 μm	>30
TES	Global Surveyor	hyperspec. (143 bands); 5.8 – 50 μm	3.15
THEMIS	Mars Odyssey	9 bands from 6.6 – 14.5 μm	0.1

Acronyms for instrument names are explained in the text. Spatial resolutions represent the typical or most common resolution.

Table 2. ASTER instrument specifications [*Abrams, 2000*].

Wavelength region	Band	Bandwidth (in μm)	Band Center (in μm)
VNIR	1	0.52 – 0.60	0.556
	2	0.63 – 0.69	0.661
	3N	0.76 – 0.86	0.807
	3B	0.75 – 0.85	0.804
SWIR	4	1.600 – 1.700	1.656
	5	2.145 – 2.185	2.167
	6	2.185 – 2.225	2.209
	7	2.235 – 2.285	2.262
	8	2.295 – 2.365	2.336
	9	2.360 – 2.430	2.400
	TIR	10	8.125 – 8.475
11		8.475 – 8.825	8.634
12		8.925 – 9.275	9.075
13		10.25 – 10.95	10.657
14		10.95 – 11.65	11.318

Table 3. TIMS instrument TIR band centers

TIR Band	Band Center
Band 1	8.45688 μm
Band 2	8.79522 μm
Band 3	9.22776 μm
Band 4	9.91665 μm
Band 5	10.79620 μm
Band 6	11.75280 μm

Table 4. THEMIS TIR and VNIR band centers

<u>Thermal Infrared:</u>			<u>Visible:</u>	
Band #	Band Center	Band Width	Band #	Band Center
1	6.78 μm	1.01	1	0.425 μm
2	6.78 μm	1.01	2	0.540 μm
3	7.93 μm	1.09	3	0.654 μm
4	8.56 μm	1.16	4	0.749 μm
5	9.35 μm	1.20	5	0.860 μm
6	10.21 μm	1.10		
7	11.04 μm	1.19		
8	11.79 μm	1.07		
9	12.57 μm	0.81		
10	14.88 μm	0.87		

Table 5. ASTER scenes of Meteor Crater, AZ

Date acquired: 16 September 2002 at 18:22:22 UTC

Level 1A	Data Granule ID : AST_L1A.003:2008443602 Local Granule ID: AST_L1A#003_09162002182222_10092002092816.hdf
Level 1B	Data Granule ID: AST_L1B.003:2008495500 Local Granule ID : AST_L1B#003_09162002182222_10102002103750.hdf
Level 2 TIR Surface Radiance	Scene ID: AST_09_003091620021822220000000.hdf

Table 6. Comparison of ASTER end-member analyses over various scales
 (Scale, in number of pixels being compared, is shown above each table)

Scale: 90 x 90 pixels (8.1 km on each side)

Image End-Member Analysis:

Sample End-Member Analysis:

<u>Image end-member:</u>	<u>Areal abundances:</u>		<u>Sample end-member:</u>
IEM#1:	5.86 %	15.87 %	Coconino Sandstone
IEM#2:	90.94 %	84.13 %	Kaibab Formation
IEM#3:	3.20 %	0.00 %	Moenkopi Formation

Scale: 36 x 36 pixels (3.24 km on each side)

Image End-Member Analysis:

Sample End-Member Analysis:

<u>Image end-member:</u>	<u>Areal abundances:</u>		<u>Sample end-member:</u>
IEM#1:	13.29 %	18.85 %	Coconino Sandstone
IEM#2:	81.35 %	81.15 %	Kaibab Formation
IEM#3:	5.36 %	0.00 %	Moenkopi Formation

Table 6 (continued)

Scale: Pixel (51, 55) – IEM#1

Image End-Member Analysis:

Sample End-Member Analysis:

<u>Image end-member:</u>	<u>Areal abundances:</u>		<u>Sample end-member:</u>
IEM#1:	100.05 %	49.10 %	Coconino Sandstone
IEM#2:	0 %	53.95 %	Kaibab Formation
IEM#3:	0 %	0.00 %	Moenkopi Formation

Scale: Pixel (40, 59) – IEM#2

Image End-Member Analysis:

Sample End-Member Analysis:

<u>Image end-member:</u>	<u>Areal abundances:</u>		<u>Sample end-member:</u>
IEM#1:	0 %	11.64 %	Coconino Sandstone
IEM#2:	100.48 %	91.31 %	Kaibab Formation
IEM#3:	0 %	0.00 %	Moenkopi Formation

Scale: Pixel (46, 58) – IEM#3

Image End-Member Analysis:

Sample End-Member Analysis:

<u>Image end-member:</u>	<u>Areal abundances:</u>		<u>Sample end-member:</u>
IEM#1:	0 %	25.04 %	Coconino Sandstone
IEM#2:	0 %	77.07 %	Kaibab Formation
IEM#3:	100.28 %	0.00 %	Moenkopi Formation

Table 7. Comparison of end-member percentages for the deconvolution using TIMS (3.2 m spatial resolution) and ASTER (90 m) data.

	TIMS:	ASTER IEMA:	ASTER SEMA:
Coconino/ IEM#1	9.11 %	14.19 %	19.47 %
Kaibab/ IEM#2	79.57 %	80.70 %	83.43 %
Moenkopi/ IEM#3	11.29 %	5.23 %	0.00 %

NOTE: Each data set covered the same region – the floor, rim, and CEB of Meteor Crater

BIBLIOGRAPHY

Abrams, M.J., The Advanced Spaceborne Thermal Emission and Reflection Radiometer (ASTER): Data products of the high spatial resolution imager on NASA's Terra platform, *International Journal of Remote Sensing*, 21, 847-859, 2000.

Bandfield, J.L, Hamilton, V.E., and Christensen, P.R., A global view of martian surface compositions from MGS-TES, *Science*, 287, 1626-1630, 2000.

Bandfield, J.L., Global mineral distributions on Mars, *Journal of Geophysical Research*, 107(E6), 10.1029/2001JE001510, 2002.

Bandfield, J.L, K.S. Edgett, and P.R. Christensen, Spectroscopic study of the Moses Lake dune field, Washington: Determination of compositional distributions and source lithologies, *Journal of Geophysical Research*, 107(E11), 5092, 10.1029/2000JE001469, 2002.

Bandfield, J.L, T.D. Glotch, and P.R. Christensen, Spectroscopic identification of carbonates in the martian dust, *LPSC XXXIV*, pp 1723, 2003.

Barlow, N.G., Updates to the "Catalog of Large Martian Impact Craters", *Lunar and Planetary Science Conference XXXI*, 1475, 2000.

Barlow, N.G., J.M. Boyce, F.M. Costard, R.A. Craddock, J.B. Garvin, S.E.H. Sakimoto, R.O. Kuzmin, D.J. Roddy, and L.A. Soderblom, Standardizing the nomenclature of Martian impact crater ejecta morphologies, *Journal of Geophysical Research*, 105, 26733-26738, 2000.

Berry, Mason, and Dietrich, *Mineralogy*, 2nd ed., 561 pp, W.H. Freeman & Co., New York, New York, 1983.

Betts, B.H. and B.C. Murray, Thermally distinct ejecta blankets from martian craters, *Journal of Geophysical Research*, 98, 11043-11059, 1993.

Carr, M.H., *The surface of Mars*, 232 pp., Yale University Press, New Haven, 1981.

Christensen, P.R., Martian dust mantling and surface composition: Interpretation of thermophysical properties, *Journal of Geophysical Research*, 87, 9985-9998, 1982.

Christensen, P.R., Regional dust deposits on Mars: Physical properties, age, and history, *Journal of Geophysical Research*, 91, 3533-3545, 1986.

Christensen, P.R., Variations in martian surface composition and cloud occurrence determined from thermal infrared spectroscopy: Analysis of Viking and Mariner 9 data, *Journal of Geophysical Research*, 103, 1733-1746, 1998.

Christensen, P.R. and H.J. Moore, The Martian surface layer, in *Mars*, edited by H.H. Kieffer et al., pp. 686-729, University of Arizona Press, Tucson, 1992.

Christensen, P.R., D.L. Anderson, S.C. Chase, R.N. Clark, H.H. Kieffer, M.C. Malin, J.C. Pearl, J. Carpenter, N. Bandiera, F.G. Brown, and S. Silverman, Thermal Emission Spectrometer Experiment: Mars Observer Mission, *Journal of Geophysical Research*, *97*, 7719-7734, 1992.

Christensen, P.R., B.M. Jakosky, H.H. Kieffer, M.C. Malin, H.Y. McSween, K. Neelson, G. Mehall, S. Silverman, and S. Ferry, The Thermal Emission Imaging System (THEMIS) instrument for the 2001 orbiter (abstract), *Lunar and Planetary Science Conference XXX*, 1470, 1999a.

Christensen, P.R., B.M. Jakosky, H.H. Kieffer, M.C. Malin, H.Y. McSween, K. Neelson, G. Mehall, S. Silverman, and S. Ferry, The Thermal Emission Imaging System (THEMIS) instrument for the 2001 orbiter (abstract), *Workshop on Mars 2001*, 2506, 1999b.

Christensen, P.R., J.L. Bandfield, M.D. Smith, V.E. Hamilton, and R.N. Clark, Identification of a basaltic component on the Martian surface for Thermal Emission Spectrometer data, *Journal of Geophysical Research*, *105*, 9609-9622, 2000a.

Christensen, P.R. et al., Detection of crystalline hematite mineralization on Mars by the Thermal Emission Spectrometer: Evidence for near-surface water, *Journal of Geophysical Research*, *105*, 9623-9642, 2000b.

Christensen, P.R., J.L. Bandfield, V.E. Hamilton, S.W. Ruff, H.H. Kieffer, T.N. Titus, M.C. Malin, R.V. Morris, M.D. Lane, R.L. Clark, B.M. Jakosky, M.T. Mellon, J.C. Pearl, B.J. Conrath, M.D. Smith, R.T. Clancy, R.O. Kuzmin, T. Roush, G.L. Mehall, N. Gorelick, K. Bender, K. Murray, S. Dason, E. Greene, S. Silverman, and M. Greenfield, Mars Global Surveyor Thermal Emission Spectrometer experiment: Investigation description and surface science results, *Journal of Geophysical Research*, *106*, 23823-23871, 2001.

Christensen, P.R., B.M. Jakosky, H.H. Kieffer, M.C. Malin, H.Y. McSween, K. Neelson, J.F. Bell, A. Ivanov, M.D. Lane, A.S. McEwen, J.E. Moersch, M.I. Richardson, and M.D. Smith, The Martian surface as seen by the 2001 Mars Odyssey Thermal Emission Imaging System Experiment, *American Geophysical Union*, abstract P11B-07, 2002.

Christensen, P.R., J.L. Bandfield, J.F. Bell, V.E. Hamilton, A. Ivanov, B.M. Jakosky, H.H. Kieffer, M.D. Lane, M.C. Malin, T. McConnochie, A.S. McEwen, H.Y. McSween, J.E. Moersch, K.H. Neelson, J.W. Rice, M.I. Richardson, S.W. Ruff, M.D. Smith, and T.N. Titus, Early results from the Odyssey THEMIS investigation (abstract), *Lunar and Planetary Science Conference XXXIV*, 1519, 2003a.

Christensen, P.R., J.L. Bandfield, J.F. Bell, N. Gorelick, V.E. Hamilton, A. Ivanov, B.M. Jakosky, H.H. Kieffer, M.D. Lane, M.C. Malin, T. McConnochie, A.S. McEwen, H.Y. McSween, G.L. Mehall, J.E. Moersch, K.H. Nealson, J.W. Rice, M.I. Richardson, S.W. Ruff, M.D. Smith, T.N. Titus, and M.B. Wyatt, Morphology and composition of the surface of Mars: Mars Odyssey THEMIS results, *Science*, 300, 2056-2061, 2003b.

Feely, K.C. and P.R. Christensen, Quantitative compositional analysis using thermal emission spectroscopy: Application to igneous and metamorphic rocks, *Journal of Geophysical Research*, 104, 24195-24210, 1999.

Garvin, J.B., R.A.F. Grieve, C. Schnetzler, and F. Honey, Geologic remote sensing of terrestrial impact craters, *Lunar and Planetary Science Conference XIX*, 375-376, 1988.

Garvin, J.B., J.L. Bufton, B.A. Campbell, and S.H. Zisk, Terrain analysis of the Meteor Crater ejecta blanket, *Lunar and Planetary Science Conference XX*, 333-334, 1989.

Garvin, J.B., C.C. Schnetzler, J.J. Frawley, and S.E.H. Sakimoto, Global geometric characteristics of fresh impact crater on Mars: A new perspective from the Mars Orbital Laser Altimeter (MOLA), *62nd Meteoritical Society Meeting*, 5135, 1999.

Garvin, J.B., J.J. Frawley, S.E.H. Sakimoto, and C.C. Schnetzler, Global geometric properties of martian impact craters: An assessment from Mars Orbital Laser Altimeter (MOLA) digital elevation models, *Lunar and Planetary Science Conference XXXI*, 1619, 2000.

Garvin, J.B., S.E.H. Sakimoto, and J.J. Frawley, Craters on Mars: Global geometric properties from gridded MOLA topography, *6th International Conference on Mars*, abstract #3277, Lunar and Planetary Institute, Houston, 2003.

Gillespie, A.R., A. B. Kahle, and F.D. Palluconi, Mapping alluvial fans in Death Valley, California, using multichannel thermal infrared images, *Geophysical Research Letters*, 11, 1153-1156, 1984.

Gillespie, A.R., M.O. Smith, J.B. Adams, and S.C. Willis, Spectral mixture analysis of multispectral thermal infrared images, in *Proceedings of the 2nd Annual Airborne Earth Science Workshop*, Volume 2, edited by E.A. Abbott, *Jet Propulsion Laboratory Publication 90-55*, 57-74, 1990.

Grant, J.A., Erosional evolution of impact craters on the Earth and Mars, Ph.D. dissertation, 401 pp., Brown University, Providence, Rhode Island, 1990.

Grant, J.A. and P.H. Schultz, Styles of crater gradation in southern Ismenius Lacus, Mars: Clues from Meteor Crater, Arizona, *MSATT Workshop*, *Lunar and Planetary Institute*, 61-62, 1992.

Grant, J.A. and P.H. Schultz, Erosion of ejecta at Meteor Crater, Arizona. *Journal of Geophysical Research*, 98, 15033-15048, 1993.

Greeley, R. and J.D. Iverson, *Wind as a Geological Process on Earth, Mars, Venus, and Titan*, 333 pp., Cambridge University Press, New York, 1985.

Hamilton, V.E. and P.R. Christensen, Determining the modal mineralogy of mafic and ultramafic rocks using thermal emission spectroscopy, *Journal of Geophysical Research*, *105*, 9717-9733, 2000.

Hanel, R.A., B.J. Conrath, W.A. Hovis, V.G. Kunde, P.D. Lowman, W. Maguire, J.C. Pearl, J. Pirraglia, C. Prabhakara, B. Schlachmann, G.V. Levine, P. Straat, and T. Burke, Investigation of the Martian environment by infrared spectroscopy on Mariner 9, *Icarus*, *17*, 423-442, 1972a.

Hanel, R.A., B.J. Conrath, W.A. Hovis, V.G. Kunde, P.D. Lowman, J.C. Pearl, C. Prabhakara, B. Schlachmann, and G.V. Levine, Infrared spectroscopy experiment on the Mariner 9 mission: Preliminary results, *Science*, *175*, 305-308, 1972b.

Hall, J.D., *Industrial Applications of Infrared*, McGraw-Hill, New York, 201 pp., 1947.

Hellman, M.J. and M.S. Ramsey, Analysis of hot springs and associated deposits in Yellowstone National Park using ASTER and AVIRIS remote sensing, *Journal of Volcanology and Geothermal Research*, in press, 2003.

Hook, S.J., K.E. Karlstrom, C.F. Miller, and K.J.W. McCaffrey, Mapping the Piute Mountains, California, with thermal infrared multi-spectral scanner (TIMS) images, *Journal of Geophysical Research*, *99*, 15605-15622, 1994.

Hörz, F., D.W. Mittlefehldt, T.H. See, and C. Galindo, Petrographic studies of the impact melts from Meteor Crater, Arizona, USA, *Meteoritics and Planetary Science*, *37*, 501-531, 2002.

Houghton, J.T. and S.D. Smith, *Infrared Physics*, Oxford University Press, Oxford, Great Britain, 319 pp., 1966.

Johnson, J.R., P.R. Christensen, and P.G. Lucey, Dust coatings on basaltic rocks and implications for thermal infrared spectroscopy of Mars, *Journal of Geophysical Research*, *107*(E6), 10.1029/2000JE001405, 2002a.

Johnson, J.R., F. Hörz, P.G. Lucey, and P.R. Christensen, Thermal infrared spectroscopy of experimentally shocked anorthosite and pyroxenite: Implications for remote sensing of Mars, *Journal of Geophysical Research*, *107*(E10), 5073, doi: 10.1029/2001JE001517, 2002b.

Kahle, A.B., F.D. Palluconi, S.J. Hook, V.J. Realmuto, and G. Bothwell, The Advanced Spaceborne Thermal Emission and Reflectance Radiometer (ASTER), *International Journal of Imaging Systems and Technology*, *3*, 144-156, 1991.

- Kendall, D.N., *Applied Infrared Spectroscopy*, Reinhold, New York, 560 pp., 1966.
- Kieffer, H.H., G. Neugebauer, G. Münch, S.C. Chase, and E. Miner, Infrared thermal mapping experiment: The Viking Mars Orbiter, *Icarus*, 16, 47-56, 1972.
- Kieffer, H.H., S.C. Chase, E.D. Miner, G. Münch, and G. Neugebauer, Preliminary report on infrared radiometric measurements from the Mariner 9 spacecraft, *Journal of Geophysical Research*, 78, 4291-4312, 1973.
- Kieffer, H.H., T.Z. Martin, A.R. Peterfreund, B.M. Jakosky, E.D. Miner, and F.D. Palluconi, Thermal and albedo mapping of Mars during the Viking primary mission, *Journal of Geophysical Research*, 82, 4249-4292, 1977.
- Leighton, R.B., B.C. Murray, R.P. Sharp, J.D. Allen, and R.K. Sloan, Mariner Mars 1964 project report: Television experiment, *NASA Technical Report 32-884*, 1967.
- Lyon, R.J.P., Analysis of rocks by spectral infrared emission (8 to 25 μm), *Economic Geology*, 60, 715-736, 1965.
- Masursky, H. An overview of geological results from Mariner 9, *Journal of Geophysical Research*, 78, 4009-4030, 1973.
- McKee, E.D., The Coconino Sandstone – its history and origin, *Contributions to Paleontology: Carnegie Institute, Washington Publication 440*, 78-115, 1934.
- McKee, E.D., The environment and history of the Toroweap and Kaibab Formations of northern Arizona and southern Utah, *Carnegie Institute of Washington, Publication 492*, 268 pp., 1938.
- McKee, E.D., Stratigraphy and history of the Moenkopi Formation of Triassic Age, *Geological Society of America Memoir 61*, 133 pp., 1954.
- Melosh, H.J., *Impact Cratering: A Geologic Process*, 78 pp., Oxford University Press, New York, 1989.
- Morton, O. *Mapping Mars*, 304 pp., St. Martin's Press, New York, 304 pp, 2002.
- Mustard, J.F., S. Erard, J.P. Bibring, J.W. Head, S. Hirtz, Y. Langevin, C.M. Pieters, and C.J. Sotin, The surface of Syrtis Major: Composition of the volcanic substrate and mixing with altered dust and soil, *Journal of Geophysical Research*, 98, 3387-3400, 1993.
- Nishiizumi, K., C.P. Kohl, E.M. Shoemaker, J.R. Arnold, J. Klein, D. Fink, and R. Middleton, In situ $^{10}\text{Be}^{26}\text{-Al}$ exposure ages at Meteor Crater, Arizona, *Geochim. Cosmochim. Acta*, 55, pp 2699-2703, 1991.

Palluconi, F.D. and H.H. Kieffer, Thermal inertia mapping of Mars from 60° S to 60° N, *Icarus*, 45, 415-426, 1981.

Ramsey, M.S., Quantitative analysis of geological surfaces: A deconvolution algorithm for midinfrared remote sensing data, 276 pp., Ph.D. dissertation, Arizona State University, Tempe, Arizona, 1996.

Ramsey, M.S., Ejecta distribution patterns at Meteor Crater, Arizona: On the applicability of lithologic end-member deconvolution for spaceborne thermal infrared data of Earth and Mars, *Journal of Geophysical Research*, 107(E8), doi:10.1029/2001JE001827, 2002a.

Ramsey, M.S., Using terrestrial multispectral images as a proxy for constraining new thermal infrared data of Mars, in *Proceedings of the Mars Infrared Spectroscopy Workshop*, 2016.pdf, Lunar & Planetary Institute., 2002b.

Ramsey, M.S., Closing the terrestrial-planetary remote sensing loop: Spectral, spatial and physical proxies, *American Geophysical Union Fall Meeting (abs. P62B-12)*, 2002c.

Ramsey, M.S. and J.H. Fink, Remote monitoring of volcanic domes: Detection of chemical, textural, and thermal heterogeneities, *Eos Transactions, American Geophysical Union*, 75, 716, 1994.

Ramsey, M.S. and P.R. Christensen, Mineral abundance determination: Quantitative deconvolution of thermal emission spectra, *Journal of Geophysical Research*, 103, pp. 577-596, 1998.

Ramsey, M.S. and J.H. Fink, Estimating silicic lava vesicularity with thermal remote sensing: A new technique for volcanic mapping and monitoring, *Bulletin Volcanology*, 61, 32-39, 1999.

Ramsey, M.S., P.R. Christensen, N. Lancaster, and D.A. Howard, Identification of sand sources and transport pathways at the Kelso Dunes, California using thermal infrared remote sensing, *Geological Society of America Bulletin*, 111, 646-662, 1999.

Realmuto, V.J., Separating the effects of temperature and emissivity: Emissivity spectrum normalization, in *Proceedings of the Second Annual Airborne Earth Science Workshop*, volume 2, edited by E.A. Abbott, *JPL Publication 90-55*, pp. 31-35, 1990.

Roddy, D.J., Pre-impact geologic conditions, physical properties, energy calculations, meteorite and initial crater dimensions, and orientations of joints, faults, and walls at Meteor Crater, Arizona, *Proceedings from Lunar and Planetary Science Conference*, Volume 9, pp 3891-3930, 1978.

- Rogers, D. and P.R. Christensen, Age relationship of basaltic and andesitic surface compositions on Mars: Analysis of high-resolution TES observations of the northern hemisphere, *Journal of Geophysical Research*, 108(E4), 5030, doi:10.1029/2002JE001913, 2003.
- Ruff, S.W., P.R. Christensen, P.W. Barbera, and D.L. Anderson, Quantitative thermal emission spectroscopy of minerals: A laboratory technique for measurement and calibration, *Journal of Geophysical Research*, 102, 14899-14913, 1997.
- Ruff, S.W. and P.R. Christensen, Bright and dark regions on Mars: Particle size and mineralogical characteristics based on Thermal Emission Spectrometer data, *Journal of Geophysical Research*, 107(E12), 5127, 10.1029/2001JE001580, 2002.
- Salisbury, J.W. and D.M. D'Aria, Emissivity of terrestrial materials in the 8-14 μm atmospheric window, *Remote Sensing Environment*, 42, 83-106, 1992.
- Salisbury, J.W. and L.S. Walter, Thermal infrared (2.5 – 13.5 μm) spectroscopic remote sensing of igneous rock types on particulate planetary surfaces, *Journal of Geophysical Research*, 94, 9192-9202, 1989.
- Shoemaker, E.M., Impact Mechanics at Meteor Crater, Arizona, Ph.D. dissertation, 55 pp., Princeton University, Princeton, New Jersey, 1960.
- Shoemaker, E.M., Impact Mechanics at Meteor Crater, Arizona, in B.M. Middlehurst and G.P. Kuiper (eds), *The Moon, Meteorites, and Comets*, Vol. 4, pp. 301 – 336, University of Chicago Press, Chicago and London, 810 pgs, 1963.
- Shoemaker, E.M. and S.W. Kieffer, Guidebook to the geology of Meteor Crater, Arizona, *Publication 17*, 66 pp., Center for Meteorite Studies, Arizona State University, Tempe, Arizona, 1974.
- Sinton, W.M., On the composition of Martian surface materials, *Icarus*, 6, 222-228, 1967.
- Thomson, J.L. and J.W. Salisbury, The mid-infrared reflectance of mineral mixtures (7-14 μm), *Remote Sensing of the Environment*, 45, 1-13, 1993.
- Van Tassel, R.A. and J.W. Salisbury, The composition of the Martian surface, *Icarus*, 3, 264-269, 1964.
- Wright, S.P. and M.S. Ramsey, End member analyses of spaceborne thermal infrared data of Meteor Crater, Arizona and application to future Mars data sets, *Solar System Remote Sensing Symposium*, LPI Contribution No. 1129, 2002.

Wright, S.P. and M.S. Ramsey, Spaceborne thermal infrared data analysis of Meteor Crater, Arizona: Analog for THEMIS data of a small impact crater in Syrtis Major, *LPSC #XXXIV*, pp 1495, 2003.